NASA/TM-20205007269

Velocity, Temperature, and Density Measurements in Supersonic Jets

Mark P. Wernet and Nicholas J. Georgiadis
Glenn Research Center, Cleveland, Ohio

Randy J. Locke
HX-5, LLC, Cleveland, Ohio

October 2020

NASA STI Program . . . in Profile

Since its founding, NASA has been dedicated to the advancement of aeronautics and space science. The NASA Scientific and Technical Information (STI) Program plays a key part in helping NASA maintain this important role.

The NASA STI Program operates under the auspices of the Agency Chief Information Officer. It collects, organizes, provides for archiving, and disseminates NASA's STI. The NASA STI Program provides access to the NASA Technical Report Server—Registered (NTRS Reg) and NASA Technical Report Server—Public (NTRS) thus providing one of the largest collections of aeronautical and space science STI in the world. Results are published in both non-NASA channels and by NASA in the NASA STI Report Series, which includes the following report types:

- TECHNICAL PUBLICATION. Reports of completed research or a major significant phase of research that present the results of NASA programs and include extensive data or theoretical analysis. Includes compilations of significant scientific and technical data and information deemed to be of continuing reference value. NASA counter-part of peer-reviewed formal professional papers, but has less stringent limitations on manuscript length and extent of graphic presentations.

- TECHNICAL MEMORANDUM. Scientific and technical findings that are preliminary or of specialized interest, e.g., "quick-release" reports, working papers, and bibliographies that contain minimal annotation. Does not contain extensive analysis.

- CONTRACTOR REPORT. Scientific and technical findings by NASA-sponsored contractors and grantees.

- CONFERENCE PUBLICATION. Collected papers from scientific and technical conferences, symposia, seminars, or other meetings sponsored or co-sponsored by NASA.

- SPECIAL PUBLICATION. Scientific, technical, or historical information from NASA programs, projects, and missions, often concerned with subjects having substantial public interest.

- TECHNICAL TRANSLATION. English-language translations of foreign scientific and technical material pertinent to NASA's mission.

For more information about the NASA STI program, see the following:

- Access the NASA STI program home page at http://www.sti.nasa.gov

- E-mail your question to help@sti.nasa.gov

- Fax your question to the NASA STI Information Desk at 757-864-6500

- Telephone the NASA STI Information Desk at 757-864-9658

- Write to:
  NASA STI Program
  Mail Stop 148
  NASA Langley Research Center
  Hampton, VA 23681-2199

NASA/TM-20205007269

Velocity, Temperature, and Density Measurements in Supersonic Jets

Mark P. Wernet and Nicholas J. Georgiadis
Glenn Research Center, Cleveland, Ohio

Randy J. Locke
HX-5, LLC, Cleveland, Ohio

Prepared for the
AIAA SciTech Forum and Exposition
sponsored by the American Institute of Aeronautics and Astronautics
Nashville, Tennessee, January 11–15, 2021

National Aeronautics and
Space Administration

Glenn Research Center
Cleveland, Ohio 44135

October 2020

Acknowledgments

This work was supported by the Transformational Tools and Technology (TTT) Project of the Transformative Aeronautics Concepts Program (TACP). The authors would also like to thank the team at the Aero-Acoustic Propulsion Laboratory (AAPL) facility for their assistance in model setup and expertise in operating the SHJAR facility. Thanks to Garrett Clayo for making the CAD renderings of the test setups and to AAPL Facility Engineer Dennis Eck who provided mechanical design layout for the Mach 2 nozzle and assisted in its fabrication.

Level of Review: This material has been technically reviewed by technical management.

Available from

NASA STI Program
Mail Stop 148
NASA Langley Research Center
Hampton, VA 23681-2199

National Technical Information Service
5285 Port Royal Road
Springfield, VA 22161
703-605-6000

This report is available in electronic form at http://www.sti.nasa.gov/ and http://ntrs.nasa.gov/

Velocity, Temperature, and Density Measurements in Supersonic Jets

Mark P. Wernet and Nicholas J. Georgiadis
National Aeronautics and Space Administration
Glenn Research Center
Cleveland, Ohio 44135

Randy J. Locke
HX-5, LLC
Cleveland, Ohio 44135

Abstract

Prediction of the flow field properties in supersonic jets using computational fluid dynamics (CFD) codes is challenging when there is a significant temperature difference between the jet core and the ambient air and/or compressibility effects are substantial. A benchmark set of flow field property data were obtained to assess current CFD capabilities and develop better modeling approaches for these turbulent flow fields where accurate calculation of turbulent heat flux is important. Three different convergent-divergent nozzles were investigated with exit Mach numbers of: 1.36, 1.63, and 2.0 at their perfectly expanded conditions. The conditions of the jet were set to obtain a temperature difference of zero between the jet core and the ambient air, and then the temperature difference was progressively increased, at the same jet Mach number. Particle Image Velocimetry (PIV), spontaneous rotational Raman scattering spectroscopy (SRS), Background Oriented Schlieren (BOS) and probe-based measurements were used to acquire high quality, spatially-resolved measurements of the mean and root mean square (rms) velocities as well as the mean and rms gas temperatures and densities in both hot and cold supersonic jet flows. The nonintrusive flow measurements are compared both against probe measurements and against standard Reynolds averaged Navier-Stokes (RANS) predictions of the supersonic jet flow properties.

The entire data set of Raman temperature and density data, along with the PIV velocity data covering the range of test points in the test matrix in Table 2 is available (from www.sti.nasa.gov) for those interested in further analysis.

Nomenclature

Acronyms:

AAPL	Aero-Acoustic Propulsion Laboratory
BOS	Background Oriented Schlieren
CFD	Computational Fluid Dynamics
GRC	Glenn Research Center
LDV	Laser Doppler Velocimetry
PIV	Particle Image Velocimetry
RANS	Reynolds averaged Navier-Stokes
rms	Root Mean Square
SHJAR	Small Hot Jet Acoustic Rig

SPIV	Stereo Particle Image Velocimetry
SRS	Spontaneous Raman Scattering
THX	Turbulent Heat Flux

Symbols:

A	Nozzle exit area [mm^2]
A*	Nozzle throat area [mm^2]
C_P	Specific heat of air [kJ/kg K]
D	nozzle diameter = 50.8 mm
D_{eff}	effective nozzle diameter for the SMC017 nozzle operated at the perfectly matched condition for the SMC014 nozzle
M	Mach number
M_{ideal}	ideally expanded jet Mach number
Pr_t	Turbulent Prandtl number
P_s	Static pressure at nozzle exit [kPa]
$P_{t,Plenum}$	Total pressure in nozzle plenum [kPa]
P_{t1}	Total pressure of the air upstream of the shock from a probe in supersonic flow [kPa]
P_{t2}	Total pressure of the air downstream of the shock from a probe in supersonic flow [kPa]
P_1	Static pressure upstream of the shock from a probe in supersonic flow [kPa]
r	Radial coordinate [mm]
R	Gas constant [J/kg K]
T′	rms temperature [K]
T_j	Temperature at jet exit [K]
$T_{t,Plenum}$	Total temperature in nozzle plenum [K]
$T_{t,j}$	Total temperature at the nozzle exit [K]
$T_{t,\infty}$	Total temperature in the ambient [K]
$T_{s,Ideal}$	Isentropically expanded static gas temperature at nozzle exit [K]
T_{SL}	Peak temperature across the shear layer [K]
T_∞	Ambient static temperature [K]
u	Axial velocity component [m/s]
u′	rms of axial velocity component [m/s]
U_j	Axial velocity component at jet exit [m/s]
v	Vertical component of velocity [m/s]
w	Spanwise component of velocity [m/s]
x	Axial distance from nozzle exit [mm]
y	Vertical coordinate from nozzle centerline [mm]
z	Spanwise distance from nozzle centerline [mm]
ΔT	Difference between jet exit temperature and ambient temperature = (T_j-T_∞) [K]
ΔT_{SL}	Difference between peak temperature across the shear layer and ambient temperature = $(T_{SL}-T_\infty)$ [K]
ΔT_t	Difference between total temperature at the jet exit and ambient temperature = $(T_{t,j}-T_\infty)$ [K]
$\Delta\rho$	Difference between ambient air density and the jet exit density = $(\rho_\infty-\rho_{Ideal})$ [kg/m^3]
$\Delta\rho_{SL}$	Difference between ambient air density and the minimum density across the shear layer = $(\rho_\infty-\rho_{SL})$ [kg/m^3]
γ	Ratio of specific heats

ρ	Gas density [kg/m^3]
ρ_f	Fluid density [g/cm^3]
ρ_{SL}	Minimum gas density across the shear layer [kg/m^3]
ρ_{Ideal}	Gas density at the nozzle exit [kg/m^3]
ρ_∞	Ambient gas density [kg/m^3]
ρ'	rms in gas density [kg/m^3]
σ_{RE}	Systematic error in the Raman temperature estimate [K]
σ_T	Measured variation in flow temperature [K]
σ_{TF}	Fluctuations in the gas temperature of the flow [K]
σ_{ME}	Measurement error in the estimated temperature from a single shot Raman spectra [K]
σ_ρ	Measurement error in the density estimates [kg/m^3]

1.0 Introduction

The objective of the Turbulent Heat Flux Step V (THX5) tests is to acquire benchmark turbulent flow field velocity, temperature and density data for round convergent-divergent nozzles. Nearly three decades ago Seiner et al. (Ref. 1) acquired centerline total pressure and temperature measurements on a Mach 2.0 round convergent-divergent nozzle at on-design (perfectly expanded) conditions. These data still remain some of the highest jet exit temperature data available in the literature and are extensively used by the jet aeroacoustics, supersonics, and even hypersonics communities to evaluate computational methods and in particular – turbulence models. Hence, the objective of this test program was to both validate and extend the available database of supersonic jet data by revisiting a Mach 2.0 round convergent-divergent nozzle that is similar to that tested by Seiner using both probes and the latest innovations in nonintrusive optical diagnostics.

Subsonic and supersonic jets have been extensively investigated using probes (temperature and pressure) and hot wires (Refs. 2 and 3). While probes can be operated over a wide range of flow conditions, hot wires are typically limited to flows below Mach 0.5. Extracting velocity data requires two different probe measurements (total pressure and total temperature) which cannot be acquired simultaneously. Further, in supersonic flows extraction of accurate velocity data requires the determination of a recovery factor to complete the data reduction (Refs. 4 and 5). Nonintrusive optical diagnostics avoid these complications in addition to not disturbing the flow. In a pioneering research effort, Lau et al. (Refs. 6 and 7) used probes, hot wires and the then newly developed Laser Doppler Velocimetry (LDV) technique to characterize subsonic and supersonic nozzle flows with both hot and cold gas exit conditions. These data were used to develop correlations of potential core length and width with respect to Mach number using the measured nozzle flows from M = 0.5 up to M = 1.67. This work established the benefits of optical diagnostics over probes, especially in supersonic flows. The nonintrusive point-based measurement techniques were soon eclipsed by planar techniques. Bridges and Wernet (Ref. 8) compiled an extensive set of velocity data using Particle Image Velocimetry to characterize the SMC000 nozzle at a series of subsonic jet Mach numbers and operating temperatures. This data has been used extensively by the jet aerodynamics and aeroacoustics CFD communities. More recently, the SMC000 nozzle was investigated using Raman spectroscopy to collect mean and rms temperatures in order to augment the existing PIV velocity data base (Ref. 9).

PIV is the defacto standard for measuring flow velocities and is readily applied in the high temperature, supersonic flow fields under study in this work (Refs. 8 and 10). While PIV systems are ubiquitous and commercially available, there are limited options for acquiring nonintrusive temperature and density measurements. Panda and Seasholtz, (Refs. 11 to 13) used spectrally resolved Rayleigh

scattering to make point measurements of velocity, temperature, and density in medium scale supersonic jet flows with very controlled conditions and a co-flow of filtered air to eliminate particulates. Rayleigh spectroscopy was also used in large-scale jet flow facilities to measure the flow parameters such as velocity, density and temperature (Ref. 14). While the velocity and density data were of good quality, the rms temperature data were of lower quality. Contamination of the measurements by entrainment of particulates in the flow compromised the quality of the Rayleigh temperature measurements. The Rayleigh technique also requires a complex optical system setup and is very sensitive to ambient light, flare light and vibration. Coherent Anti-Stokes Raman Spectroscopy (CARS), an optical technique requiring precise alignment of three coincident laser beams, has been used to obtain average temperature in high speed and reacting flows. The CARS technique is also plagued by a very complex optical setup and associated alignment issues, thereby requiring the laser to be remotely located in a climate-controlled room (Refs. 15 and 16). Transient Grating Spectroscopy (TGS) has also seen recent application to temperature measurement. While this technique has seen some success in temperature measurement within jet flows (Ref. 17), it too suffers from a complex optical setup requiring precise alignment of multiple laser beams and as such is not amenable to large scale, outdoor facilities. Vibrational and rotational Raman spectroscopy are inelastic scattering techniques that have been used quite successfully to perform temperature measurements on a variety of flows. Single-shot vibrational Raman thermometry has been performed in flames (Ref. 18) where a fast-optical shutter was used to minimize flame emission, which would otherwise obscure or interfere with the SRS spectrum. Vibrational Raman is ineffective in low temperature regimes due to the lack of the anti-Stokes bands; however, pure rotational Raman spectroscopy, which is not dependent upon anti-Stokes lines, has been used to interrogate the temperature of expanding supersonic flows of CO_2 (Ref. 19). Rotationally resolved Raman has more recently been used to acquire mean and rms temperature measurements in high temperature flows, from subsonic to supersonic speeds in harsh, real-world test facilities (Ref. 9). Rotationally resolved Raman scattering is the only technique that is relatively simple to setup/align and is robust against the hostile environments found in real world aerospace simulation facilities; therefore, it was the technique of choice for measuring the gas temperatures in supersonic jet flows of interest. Additionally, the Raman temperature measurement diagnostic was extended in this work to also extract density data from the acquired Raman spectra.

The Consensus data set of PIV, LDV and probe measurements is widely used for CFD development (Ref. 10). The recent addition of Raman temperature measurements on round subsonic nozzles extends the utility and value of the database. Having demonstrated the Raman-based temperature measurement technique on subsonic flows, it is now prudent to apply it to the more challenging problem of supersonic nozzle flows. Advocacy from the CFD community is the main motivation for this work, in order to validate and extend the limited database of supersonic jet measurements, upon which they have based their code development for the past 30 years. Traditional measurement techniques (pressure transducers and hotwire anemometry), and specifically those for temperature (thermocouples and hotwires), typically cannot survive in the hostile high-temperature, high velocity flows of relevance. They are either severely restricted in temporal response, suffer from limited spatial resolution, or have a limited lifespan once in contact with the flows. Their accuracy is also questionable since they are intrusive to the flow and as such disturb and alter the very phenomenon that they are attempting to measure. Nonintrusive measurement techniques are the preferred approach for measuring the flow-field properties under consideration here.

In addition to repeating centerline probe surveys of pressure and temperature performed by Seiner et al. (Ref. 1), the objective of this work is moreover to apply modern nonintrusive diagnostics (BOS, PIV, Raman temperature and density measurements) in an attempt to improve the quality and breadth of the database of measurements in these types of flows. The nonintrusive diagnostics provide both mean and rms measurements of the flow properties. PIV provides planar flow field measurements, yielding high

spatial resolution measurements of a large region of the flow field. The Raman point-based diagnostic is used to acquire centerline, lip-line and radial profiles, thereby extending the range of the flow field that is measured beyond just the jet centerline. The new, modern diagnostic results are compared to probe measurements, and in turn compared to the "historical" results of Seiner, for the cases where Mach 2.0 nozzle jet temperatures can be replicated in the SHJAR facility. In order to broaden the database for supersonic nozzles, Mach 1.36 and Mach 1.63 convergent-divergent nozzles were also tested as listed in Table 2. The matrix of flow conditions for this test is constructed to systematically investigate the effects of temperature and Mach number on the flow fields. A database of measurements, where only a single parameter is varied provides an invaluable resource for CFD prediction capability assessment and accurate turbulence model development.

2.0 Project Description

NASA's Turbulent Heat Flux (THX) task under the Transformational Tools & Technologies (TTT) project has been focused on acquiring benchmark velocity and temperature data in turbulent shear layers for validation of computational fluid dynamics (CFD) codes. The experiments described in this report are one in a series of recent TTT-sponsored efforts, where the turbulent transport of heat is a dominant aero-thermodynamic feature. While these previous TTT-sponsored efforts focused on subsonic film-cooling flows (Refs. 20 and 21), the current work is focused on unheated and heated supersonic jets. Standard CFD turbulence models lack the ability to accurately calculate a number of fundamental flow phenomena, including the turbulent transport of heat. In nearly all production class Reynolds-averaged Navier-Stokes (RANS) CFD codes, a gradient-diffusion approximation is applied whereby a constant turbulent Prandtl number, Pr_t, is used to relate an eddy viscosity calculated for the momentum terms to the turbulent thermal diffusivity for the turbulent heat flux terms. The default setting in many CFD codes use $Pr_t = 0.9$, which is believed to be more accurate for wall bounded flows, however; this is not representative of all flows. As discussed in Yoder (Ref. 22) and Reynolds (Ref. 23), $Pr_t = 0.7$ is frequently considered a more appropriate single value choice for jets, but is also believed not to be a constant across the entire flow field. Recent work, as discussed in Yoder (Ref. 24), has explored more complex formulations, including variable turbulent Prandtl number models, but results have not generated significant improvement over the constant Pr_t approach. A key difficulty in developing more accurate models for the turbulent heat flux is the lack of experimental data that quantify the turbulent thermal state. PIV provides planar measurements of the flow field mean and rms velocities. The Raman temperature measurement grid includes centerline, lip-line and radial profiles, significantly adding to the characterization of the supersonic flows, especially in the regions of high turbulence and heat transfer. The acquired data should be useful for assessment and improvement of CFD turbulent calculation methods since regions of high turbulence are assumed to be the regions of peak fluctuations in temperature. Additionally, these supersonic jet flows contain interacting streams of gas at different temperatures moving at different velocities, thereby exhibiting both momentum and thermal transfer processes, which must be accurately modeled via CFD.

3.0 AAPL Laboratory, SHJAR, and Experimental Setup

The Aero-Acoustic Propulsion Laboratory (AAPL) at the NASA Glenn Research Center was selected for this test due to the existing supersonic nozzles available, the rig's hot flow capabilities, the availability of probe measurements, and the ability to perform PIV and Raman optical diagnostics measurements. While probe measurements are readily implemented, the AAPL has a number of features that make implementing optical diagnostics a challenge: 1) The AAPL is open to the outside environment and as

such can experience large temperature variations over the course of a day-long test, 2) High sonic noise levels upwards of 115 dB, 3) High ambient light levels due to the large, 17 m wide by 11 m high exhaust-door which must remain open during tests, and 4) Inaccessibility by personnel during the tests.

All the data presented herein were obtained on the Small Hot Jet Acoustic Rig (SHJAR) located within the AAPL at NASA GRC. The AAPL (Figure 1) is a 19.8 m radius geodesic dome with its interior walls covered by sound absorbing wedges providing a near anechoic environment. The SHJAR (Figure 2) is a single flow stream free jet rig capable of producing jets operating fully expanded up to Mach 2 at jet static temperature ratios up to approximately 2.8. The centerline of the nozzle exit of the SHJAR is 3 m above the floor. Vitiated flow heated up to 950 K is provided by an inline hydrogen combustor and supply air is provided by central compressor facilities, permitting continuous operation. The fuel-air mass-flow ratios for heating the supply air ranged from 1.3×10^{-3} to 8.2×10^{-3} resulting in a few percent change in the nitrogen to oxygen ratio of the heated air at the nozzle exit, but not large enough to cause any significant difficulties in processing the acquired Rotational Raman spectra and extracting gas temperature estimates.

In order to replicate the work of Seiner et al. (Ref. 1), a new supersonic nozzle was fabricated that has the same internal contour as the perfectly expanded nozzle used by Seiner, yet is scaled down from a 91.44 mm (3.6 in.) exit diameter to a 50.8 mm (2.0 in.) exit diameter. Further, the nozzle was designed in the same philosophy as the long-running series of nozzles tested in the SHJAR known as the simple metal chevron, or SMC series of round nozzles (Refs. 8 and 10). All of these nozzles have an exit diameter of 50.8 mm. The initial nozzle designated as SMC000 was a convergent only reference nozzle. In later work at NASA GRC, supersonic nozzles up to a perfectly expanded Mach number of 1.8 were designed, fabricated and tested in PIV measurement campaigns as discussed in Bridges and Wernet (Ref. 25). Of particular interest are: 1) the SMC015 nozzle, which has a perfectly expanded Mach number of 1.36, and 2) SMC017, which has a perfectly expanded Mach number of 1.63. In the current test program, these two existing nozzles were studied along with the new Mach 2.0 nozzle, which is designated SMC020.

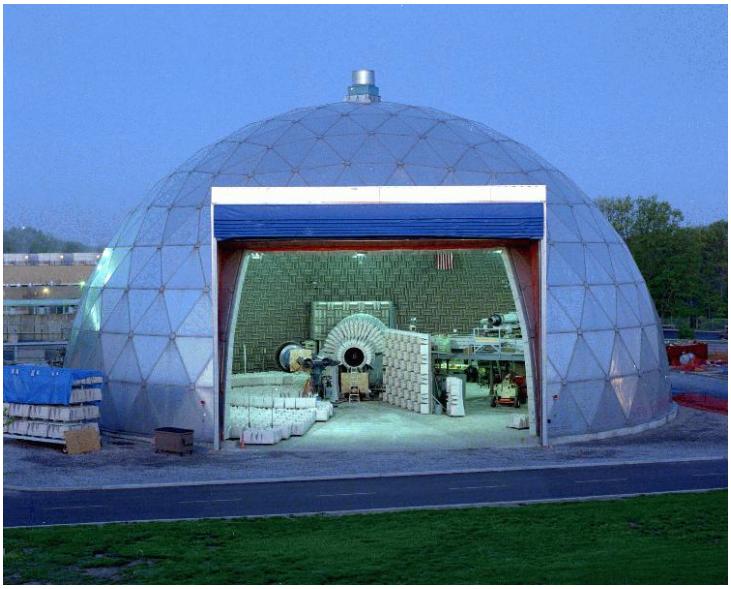

Figure 1.—Photograph of the AAPL laboratory. SHJAR is the smaller rig to the left of center.

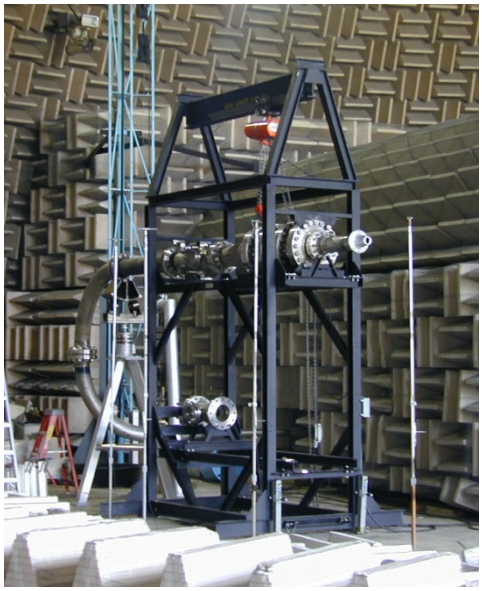

Figure 2.—Photograph of the SHJAR facility.

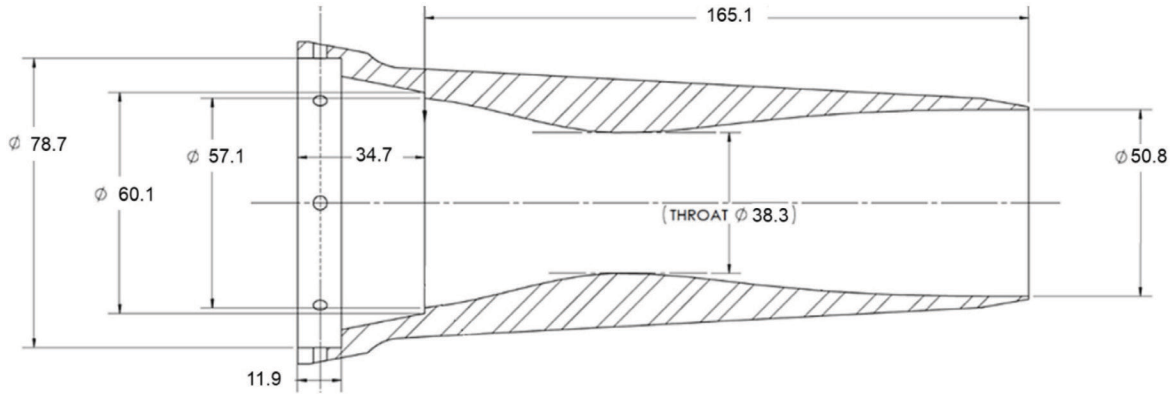

Figure 3.—SMC020 nozzle section view illustrating the interior convergent-divergent nozzle surface. All units are in millimeter.

A cross-sectional view of the new Mach 2.0 nozzle (SMC020) is shown in Figure 3. The convergent section was selected to match the slope of an existing adapter piece used for round nozzles with the SHJAR, and to allow the entire nozzle to have an overall length from the plane joining the adapter piece to the nozzle exit of 165 mm (6.5 in.), so that it matched the length of the existing SMC015 and SMC017 nozzles.

Normally the SHJAR mass flow is determined using the pressure behind a calibrated Venturi orifice. For the new Mach 2 nozzle, the pressure drop across the Venturi plate would preclude reaching the requisite plenum pressure for matching some of the Seiner set points. Hence, the Venturi orifice plate was replaced with a bleed ring fitted with a hot-wire based mass flow meter, thereby mitigating the large pressure drop across the orifice plate for these tests. The mass flow meter was calibrated in-house at NASA GRC over the full range of mass flows to be studied during the THX5 test program.

4.0 Pure Rotational Raman Temperature Measurements

Rotationally resolved Raman scattering has been previously used to measure gas temperature in heated high-speed jet flows in the SHJAR facility at NASA GRC (Ref. 9). A thorough discussion of Raman spectroscopy theory and practices can be found in Ferraro and Nakamoto (Ref. 26). In general, Raman scattering is an inelastic process, with a signal intensity approximately 10^{-3} times that from Rayleigh scattered light. Raman scattering is not dependent on wavelength but is linear with respect to the species number density and is species specific by virtue of the quantization of individual molecular energy states. In this work, the composition of the gas is known (heated air) and only the gas temperature is being measured, which greatly simplifies the data analysis and reduction.

The key features in the layout of the Raman temperature diagnostic are shown in Figure 4. A 10 Hz Continuum long-pulse length Agilite Nd:YAG laser with 600 mJ of energy at 532 nm spread across 200 nsec was used to probe the flow temperature and density while still avoiding breakdown of the gas. The 9 mm diameter output beam was focused by a 500 mm spherical lens to a roughly 70 μm beam waist. In order to maximize the collected rotational Raman scattered signal, a pair of 135 mm Nikon collection lenses set at f/4 and equipped with 42 mm extension tubes were used to collect the scattered light. The lenses were vertically mounted and focused on the laser beam focal volume approximately 257 mm distant. Each lens was displaced from the horizontal plane and tilted (upper –8.5°, lower +8.5°), which is the closest the lenses could be mounted side-by-side.

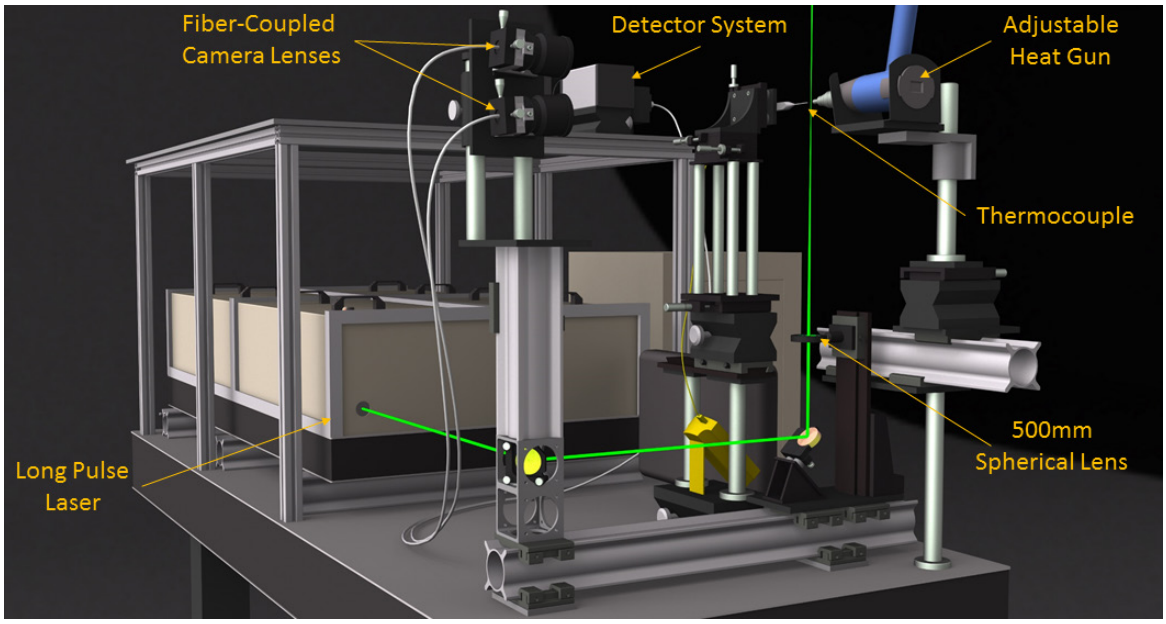

Figure 4.—Rendering of the Raman system configuration in the lab for obtaining the temperature calibration.

The light captured by each lens was passed through a 532 nm RazorEdge long-pass 24.5 mm filter attached to the rear of each camera lens mount. The filtered light was focused onto a bifurcated fiber bundle from Fiberoptic Systems, Inc. The input ends of the bifurcated fiber bundle each contained fifty-seven 100 μm diameter cladding-free fibers which were formed into a linear array at the output end of the bundle. The input end of the collection fiber bundles had the fibers arranged in an ordered array of concentric rings. The outer most ring of fibers at the collection end was oriented at the top of the linear array end of the fiber (entering the spectrometer). The 2nd outer-most ring of fibers on the collection end of the bundle was then positioned just below the first set of fibers in the linear output. The linear fiber bundle output was coupled to the entrance slit of an Acton 500 mm imaging spectrometer with an 1800 groove ruled grating and a wavelength centerline of 537 nm resulting in a spectral wavelength span of approximately 12 nm. The slit of the spectrometer was opened to its maximum of 2.0 mm allowing the fibers to act as their own 100 μm slit. A PI-MAX2 ICCD camera with an 18 mm diameter gated intensifier from Princeton Instruments was coupled to the exit of the spectrometer and the resultant rotational Raman spectra captured using Princeton's WinSpec32 software. In order to verify alignment of the 532 nm laser beam with the focus of the two camera lenses, a 635 nm diode laser was fiber-coupled to the rear of the two 135 mm collection lenses and directed back to the probe volume. Here, the alignment of all three components of the measurement system could be visually confirmed by the intersection of the back projected/focused diode laser beams. The Raman measurement volume is defined by the intersection of the Nd:YAG laser beam diameter and the two 135 mm lens collection cones. The length of the 70 μm diameter laser beam collected by the 135 mm lenses is defined by the size of the fiber bundle used to collect and transmit the light to the spectrometer. The entrance face of each of the fiber bundles is 0.85 mm in diameter. The 135 mm lenses image a 1.2 mm length of the laser beam onto the face of the fiber bundle. The resulting cylindrical probe volume used in this work is 4.5×10^{-3} mm^3. Due to the ordered array of fibers on the inlet and output ends of the fiber-optic bundle, the effective size of the probe volume could be adjusted in software by restricting the region of interest of the CCD image from the spectrometer used in the data processing. If the outer ring is cropped in the data processing, the probe volume length is reduced to 1.0 mm. If the two outer rings are cropped, the probe volume length is reduced to 0.7 mm. For this work, the full image area on the CCD sensor was used, i.e., a 1.2 mm long probe volume.

4.1 Raman Data Processing: Temperature

Estimates of the gas temperature were extracted from the acquired rotational Raman spectra using an iterative process, which determines the best fit between the measured spectrum and the spectrum computed using a pure-rotational Raman scattering model. The data reduction process is described in more detail in Locke et al. (Ref. 9). The Raman scattering spectrum model assumes that the gas composition is a mixture of only molecular nitrogen and oxygen, which is justified since the measurements were made in air and other atmospheric gaseous components do not contribute significantly to the Raman signal. For a given temperature, the model computes Raman line locations and strengths in the Raman Stokes (S) bands of nitrogen and oxygen up to rotational quantum numbers of 50. The merged array of Raman lines for N_2 and O_2 with their respective strengths and wavenumbers, was then convolved with a Voigt kernel derived from the spectral profile of the pump laser wavelength peak as measured through the optical system.

In the data processing stage, 1000 single-shot spectra acquired at each measurement location, were read into a MATLAB (The MathWorks, Inc.) based data reduction software. In each acquisition sequence, there are typically several bad spectra due to the wait time of the spectrometer camera's image intensifier. Additionally, there were times when particulates in the flow passed through the measurement volume producing strong signals at the laser line wavelength, yielding Rayleigh/laser line peaks of higher intensity than the Raman signal. In order to remove these spurious spectra, the data set was sorted to remove the 10 highest amplitude spectra. The number of particulate contaminated spectra removed was adjusted according to the number of particles present during the data acquisition. Hence, a maximum of 990 single shot spectra were used in each ensemble.

The 990 spectra were then used to compute an average spectrum, which was fit to the O_2/N_2 model function using a combined genetic algorithm for the global search, followed by a local search using a nonlinear least squares (NLLS) routine. The model parameters used in the fit included the temperature, the Raman signal amplitude, the kernel width (a 2-parameter Voigt instrument function) and the spectrometer grating calibration parameters, which included the laser-line center location. The fit of the mean spectra provided the initial estimates for all of the single shot spectral fits. The estimated temperatures from the processed spectra were then used to compute the mean temperature estimate and the rms temperature across the ensemble, T′. The time to process the 990 spectra was on the order of 1 min on a 20-core CPU. A sample averaged spectrum acquired at a gas temperature of 547 K and its corresponding fit are shown in Figure 5.

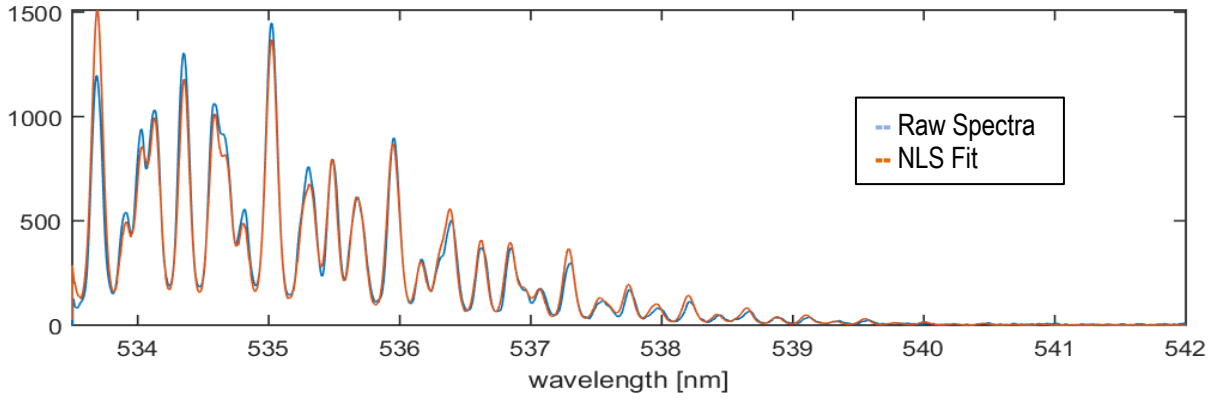

Figure 5.—Sample averaged rotational Raman temperature spectrum with fit for a gas temperature of 547 K.

4.2 Raman Data Processing: Density

The acquired Raman spectra also contained information about the density of the gas in the probe volume at the time of the measurement. The collected signal energy was proportional to both the laser power and the number of scattering molecules in the probe volume at the time of the measurement. Normalizing the measured Raman signal level or the area under the Raman spectra by the energy in each laser pulse yields a measurement proportional to the gas density. A photodiode was placed near the laser exit aperture to collect light from each laser pulse. A sampling plate was not required as there was sufficient scattered light at the laser exit. The photodiode signal was digitized using a PicoScope high-speed digitizer. A C++ program was written to control the acquisition of the PicoScope, which was synchronized to the laser pulse output using the PI-Max2 camera intensifier gate pulse as a trigger signal. The time-base and voltage range of the A/D converter and the number of samples to be recorded were selected by the user. The program also integrated the area under each of the acquired laser pulses. Both the raw data from each laser pulse and the integrated area were written to separate files, which were coordinated with the Raman spectra file naming.

4.3 Raman System Calibration

The Raman technique samples the molecules in the probe volume in order to estimate the gas temperature. The molecules in the probe volume can have any one of a number of states as defined by the Boltzmann distribution. The number of populated states increases with temperature, hence the rms temperature increases with increasing temperature of the gas. This is a known and documented characteristic of the technique, which is actually a systematic measurement error (Ref. 9). A calibration of the Raman system in a well characterized environment free from flow turbulence of other noise sources is required in order to characterize this inherent rms temperature variation in the technique. A lab scale setup using the concentrated output from an electrical heat gun calibrated using a thermocouple was used to acquire the calibration data (Ref. 9). The Raman spectra acquired at the 11 different temperature settings on the heat gun were processed according to the procedures described in the preceding data reduction discussion. The ensemble of 990 measurements at each point were used to compute the mean and rms gas temperature. Figure 6 plots the mean temperature of all 990 accumulated spectra along with the rms error bars at each temperature. The mean calibration temperature measurements were found to be accurate to <0.2 percent over the range of 296 to 850 K. Here accuracy was defined as the deviation of the measurement from the true (known) value. For these calibration measurements, the mean temperature level was measured using a 0.635 mm diameter sheathed-thermocouple. The reported error is the deviation of the Raman based mean temperature measurement from the thermocouple measurements. A full system calibration was required for each new configuration of the Raman diagnostic system.

The Raman based calibration rms temperature estimate is ±1.6 percent at 296 K and ±3.1 percent at 850 K. The Raman temperature measurements reported here illustrate the best-case measurement accuracy that can be expected using the Raman thermometry diagnostic. The Raman measurements contain three main contributions to the rms variations: 1) random measurement error σ_{ME}, 2) thermal fluctuations in the gas σ_{TF}, and 3) systematic error in the Raman diagnostic σ_{RE}, as shown in Equation (1). These error sources add in quadrature to yield the total rms variation in the measured temperature. The large ensemble of 990 was used to drive down the random measurement error by $1/\sqrt{N}$. Larger samples sizes were collected, but yielded no further reduction in the observed rms variations. Dynamic thermocouple measurements in the heat gun flow showed that the σ_{TF} is negligible for the calibration measurements (Ref. 9). Hence, the remaining contribution to the observed rms variation was the inherent systematic error in the Raman technique.

$$\sigma_T^2 = \sigma_{ME}^2 + \sigma_{TF}^2 + \sigma_{RE}^2 \quad (1)$$

The calibration plot error bars in Figure 6 clearly illustrate that the measured rms increases linearly with temperature, as stated above. A linear fit to the rms temperature as a function of the known temperature, yields a relation for the expected systematic error in the Raman based temperature diagnostic:

$$\sigma_{RE} = 0.0337\,T - 4.4816\,K \quad (2)$$

This expression will be used later to correct the expected systematic error resulting from the Raman temperature measurement technique when the rms temperature measurements in the heated jet plume are processed.

Density calibrations were also required in order to convert the measured area under the fitted Raman spectra into physical units of density. The density calibrations were obtained using a cross-shaped stainless-steel pressure vessel equipped with four window ports, as shown in Figure 7. Known conditions in the vessel at elevated pressures and temperatures were used to obtain the calibrations. The Agilite laser beam passed through the tilted window ports in the chamber to avoid back reflections. The collection lenses were aligned on either side of a perpendicular set of window ports to collect the Raman scattered light. The vessel was wrapped with electrical heating-tape and insulated to reduce heat loss through the metal surfaces. A thermocouple, inserted near the center of the vessel, provided gas temperature measurements essentially at the Raman-system probe volume location. The pressure in the vessel was measured using a Heise digital pressure gauge. As a demonstration of the linearity of the density measurements of the Raman diagnostic, Raman spectra were collected across a range of pressures and temperatures. For each survey, the temperature in the vessel was held constant while the pressure in the

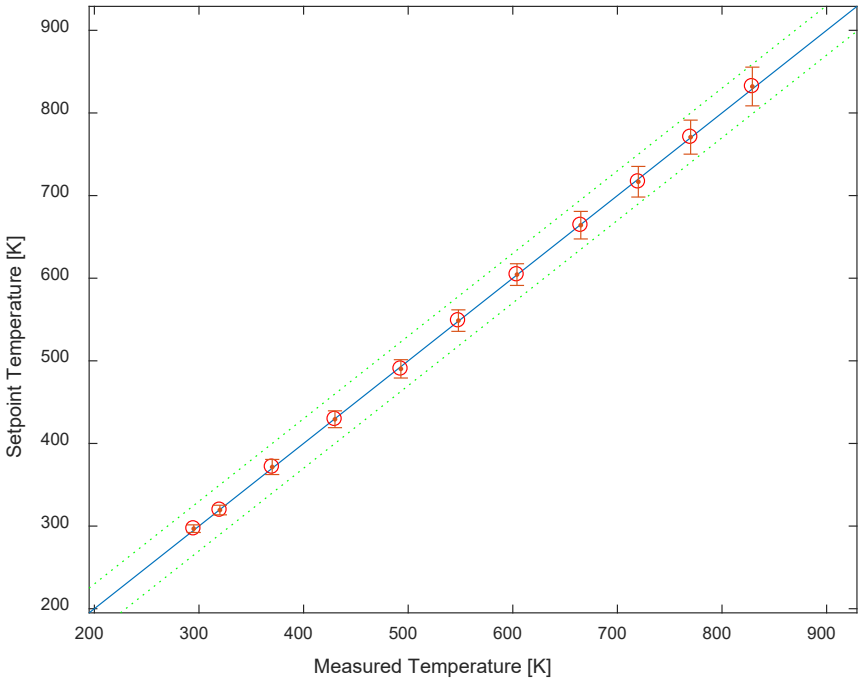

Figure 6.—Plot comparing the thermocouple reading versus the calculated temperature and the RMS variations in temperature (plotted as error bars) over the range of calibration temperatures.

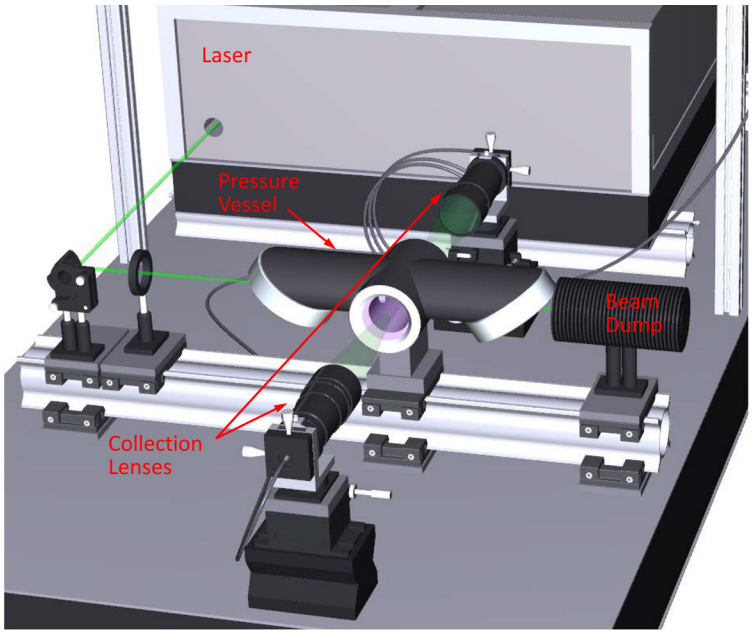

Figure 7.—Density calibration rig setup in the lab.

chamber was brought up from a vacuum to approximately 365.4 kPa (53 psia). The collected Raman spectra were first processed to extract the gas temperature. The Raman spectra were then integrated and normalized by the laser-pulse energy, in order to estimate the gas density. The processed density data are plotted as a 3D scatter plot in Figure 8(a), where the vertical axis is the measured mean density, the horizontal axis is the set point density in the vessel and the transverse axis is the temperature in the vessel. The line colors correspond to the temperature setting in the vessel and the color of the symbols along each line are color coded to the measured gas density, as shown in the plot legends. The range of temperatures covered was 294 to 750 K and the pressure in the vessel covered the range of 1.378 kPa (0.2 psia) to 365.4 kPa (53 psia). The scatter plot illustrates the linear relationship between the gas density in the vessel and the normalized Raman signal energy. The ensemble of density estimates mirrors the Raman temperature measurement ensemble; hence 990 measurements were used to compute the mean and rms density fluctuations. The measured densities are plotted against the pressure in the vessel in Figure 8(b). The rms variation in the densities are plotted as error bars on the plot. The relative rms variation in gas density is nominally between 1 to 2 percent over most of the range, increasing to 3 to 7 percent below 50 kPa. The error in the estimated density, σ_ρ, relative to the known conditions in the vessel are listed in Table 1. The lowest relative error is at the highest pressure and lowest temperature. The highest relative error is at the lowest pressure and highest temperature condition, where the deviation of the measured density from the known density is not particularly large, however; the absolute density at this condition is very low, yielding the high relative error. The gas in the pressure vessel is assumed to be at isotropic conditions, hence, these plots yield an indication of the error in the density estimates across the full range of conditions measured. The lowest density expected in the jet core measurements in the SHJAR is about 0.5 kg/m^3, corresponding to approximately 50 kPa in Figure 8(b). Hence, the nominal relative error in the density should be <4 percent over the expected range of test conditions in the SHJAR.

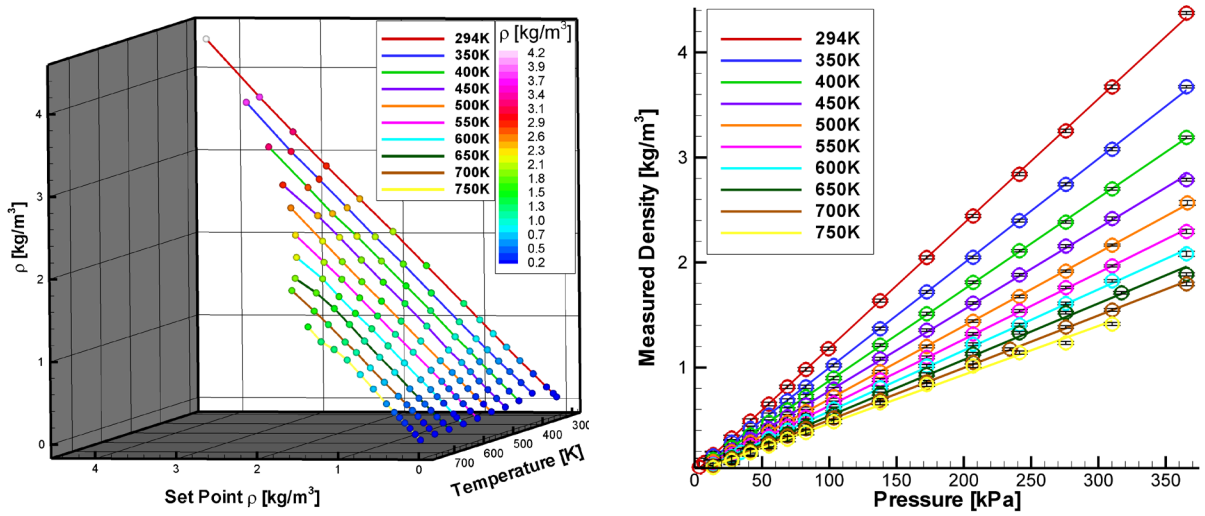

Figure 8.—(a) Raman system density calibration results using a pressure vessel in the lab; (b) Measured gas densities plotted against the set point with the rms density plotted as error bars at each point.

TABLE 1.—RELATIVE ERROR IN THE DENSITY ESTIMATES

	σ_ρ/ρ at 300 K, percent	σ_ρ/ρ at 750 K, percent
13.789 kPa (2 psi)	3	28
101.352 kPa (14.7 psi)	0.5	4
310.264 kPa (45 psi)	0.2	2

When acquiring data in the SHJAR facility, density calibrations were performed using measurements of the ambient air density before the run day began, combined with Raman measurements acquired near the nozzle exit. The conditions at the nozzle exit were computed using the plenum gas temperature and pressure along with the temperature compensated ratio of specific heats, γ. The composition of the gas due to the combustion of the hydrogen fuel was also used in the computation of γ and the estimated gas density at the nozzle exit, ρ_{Ideal}.

4.4 Raman System Installation in SHJAR

The optical excitation and detection system used to acquire the Raman temperature calibration in the laboratory was also used to acquire the nozzle test data in the AAPL. The long-pulse, Agilite laser, beam insertion optics, detection optics and spectrometer/camera detection systems were transported, installed, and aligned in the AAPL as shown in Figure 9. Due to its large size, the Agilite laser head had to be mounted inside the frame of the large traverse system. Additionally, the laser head was placed inside of a protective enclosure constructed of metal framing and insulated Plexiglas panels, which is depicted in Figure 9. The THX5 test was conducted in the fall of 2019, with ambient temperatures dropping to 270 K in the early morning. The laser head enclosure was fitted with electric blankets and additional insulation in order to keep the laser head temperature consistently at 305 K. The beam exiting from the laser was directed towards the front face of the large traverse where it was turned vertically using a mirror. A catching mirror then turned the laser beam horizontal and parallel to the front face of the large traverse.

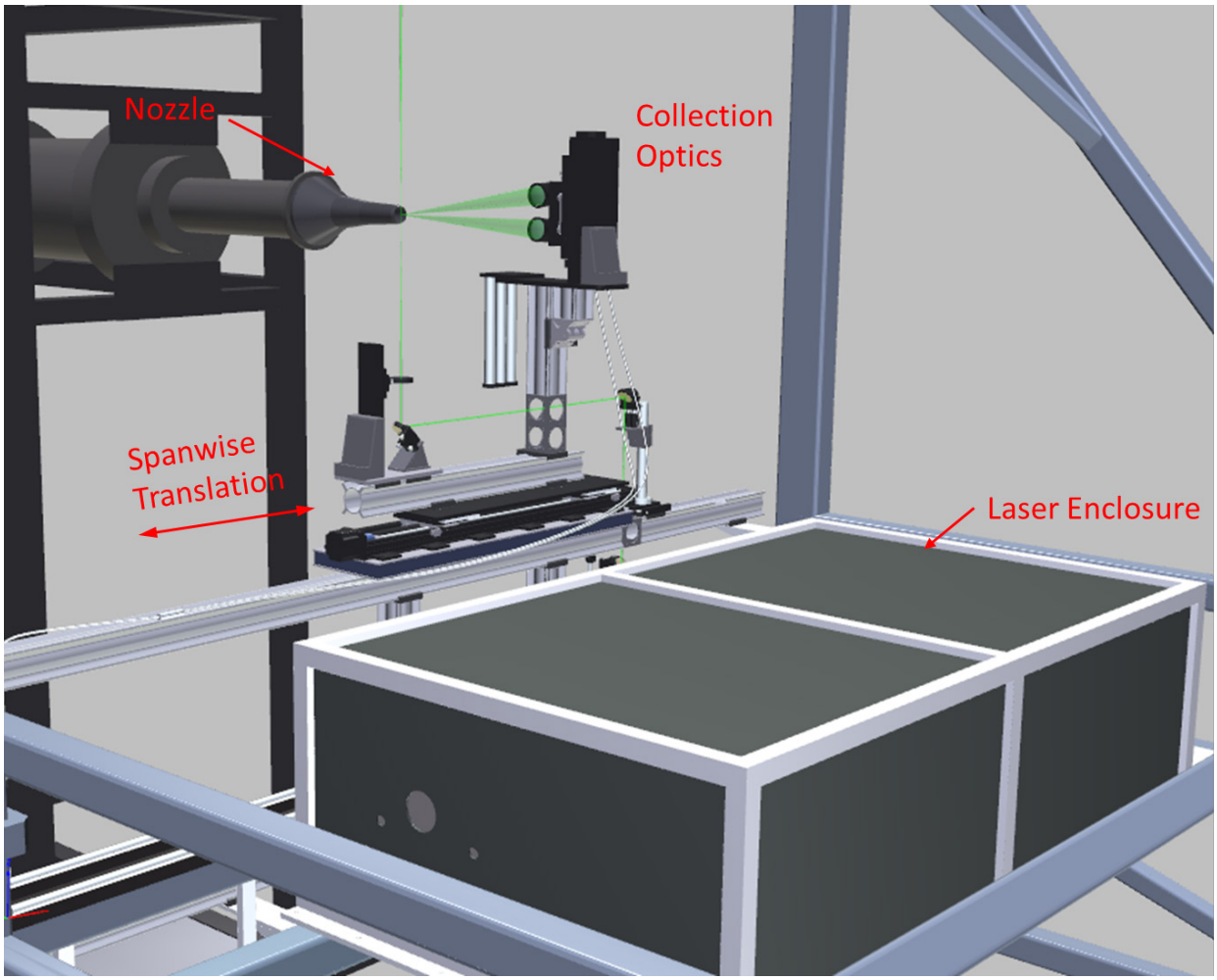

Figure 9.—SHJAR and large traverse loaded with the long-pulse laser and Raman collection optics. The Agilite laser is located within the black enclosure.

A final turning mirror directed the laser beam vertical so that it passed vertically through the jet flow field. A 500 mm focal length spherical lens then focused the beam at the center of the flow, downstream of the nozzle's exit plane. The final turning mirror, lens and the camera collection lenses were mounted on a Velmex translation stage, which provided the spanwise surveys of the jet plume. The vertical position of the measurement volume was located at the waist of the focused laser beam, which was positioned at the centerline of the nozzle exit.

5.0 PIV Measurement System

For the PIV portion of the measurement campaign, data were acquired using two different PIV configurations: one mapping cross-stream planes, with the cameras mounted in a stereo configuration to obtain 3-component (3C) of velocity; and another mapping the nozzle centerline plane using a dual side-by-side camera configuration to obtain 2-components (2C) of velocity.

5.1 3C SPIV Configuration

The Stereo Particle Image Velocimetry (SPIV) system was configured to provide cross-stream measurements of the 3-component (3C) velocity field from the test article. The entire SPIV system was mounted on the large traverse system to perform surveys of the flow field as shown in Figure 10. The travel range of the traverse was approximately 2.133 m, with a positioning accuracy of 1 mm. The SPIV system employed two high-resolution (4008×2672 pixel) cameras equipped with 180 mm focal length lenses and 8 mm extension tubes, to provide a 454×380 mm (W×H) field-of-view. The cameras were mounted downstream of the model exit plane at nominally ±45° from the nozzle centerline. Both cameras were connected to a single computer system via a CameraLink PCI card and the 400 frame pair data sequences were acquired and streamed to disk at a rate of 2 frame pairs/camera/sec. Stereo PIV calibrations were performed using a single plane target translated to 9 axial positions over a ±2 mm range. A 3rd order polynomial was used in the image de-warping and a calibration verification operation was employed to ensure that the calibration overlapped the laser light sheet plane. The SPIV measurement plane was illuminated using a dual head 400 mJ/pulse Nd:YAG laser system. The light sheet forming optics were mounted below the model yielding a vertically diverging, 1 mm thick light sheet filling the SPIV cameras' fields-of-view. The axial locations measured were: 25.4, 50.8, 101.6, 203.2, 304.8, 496.4, 508.0, 609.6, 812.8, and 1016.0 mm from the exit plane of the nozzle.

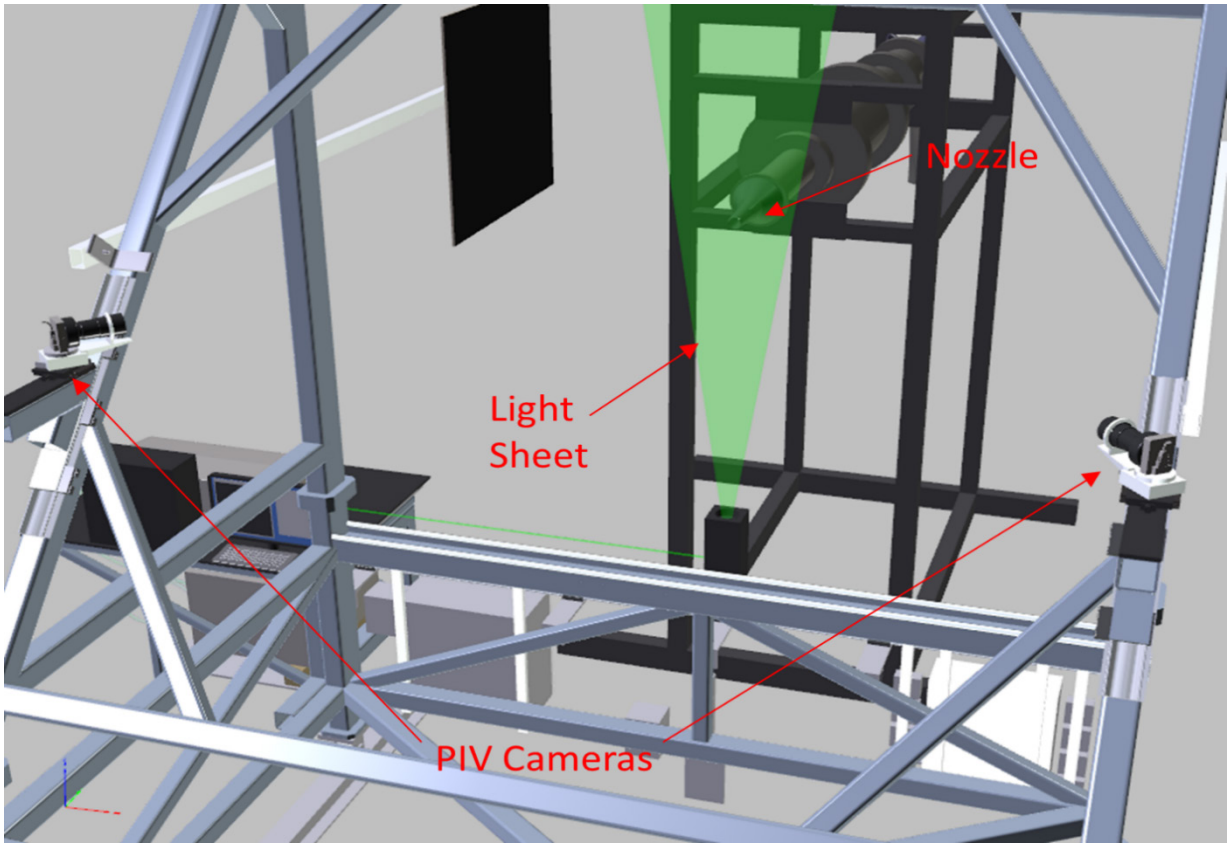

Figure 10.—Cross-stream Stereo PIV installation on the large traverse system in the SHJAR.

5.2 2C Streamwise PIV Configuration

A standard PIV system was used to measure the 2-component (2C) streamwise velocity field down the centerline of the nozzle. In order to maximize the field-of-view, while maintaining high spatial resolution PIV vector maps, a dual side-by-side camera configuration was used to acquire the centerline streamwise plane of data, as shown in Figure 11. The pair of ES11000 cameras (4008×2672 pixels) were equipped with 135 mm focal length lenses and 8 mm extension tubes and positioned so that their fields-of-view overlapped by 25.4 mm. The cameras were mounted in portrait mode (4008-pixel axis oriented vertically) yielding two 200×300 mm (W×H) imaged fields-of-view, which when combined yielded a 355×300 mm field-of-view. The PIV measurement plane was again illuminated using a dual head 400 mJ/pulse Nd:YAG laser system with the laser beams formed into vertically diverging 1 by 300 mm wide light sheets using cylindrical and spherical lenses. A flat, SPIV-style calibration target was used to calibrate and register the two cameras using a fiducial mark in the overlapping region of each cameras' field of view. The physical registration of the two cameras was used in the setup of the vector processing grids in the left and right camera images so that no interpolation was required in the merging of the left/right vector maps. The PIV system was used to map the centerline flow field by traversing in four, 300 mm increments, providing overlapping processed vector maps that were merged into a single 300×1220 mm processed vector map.

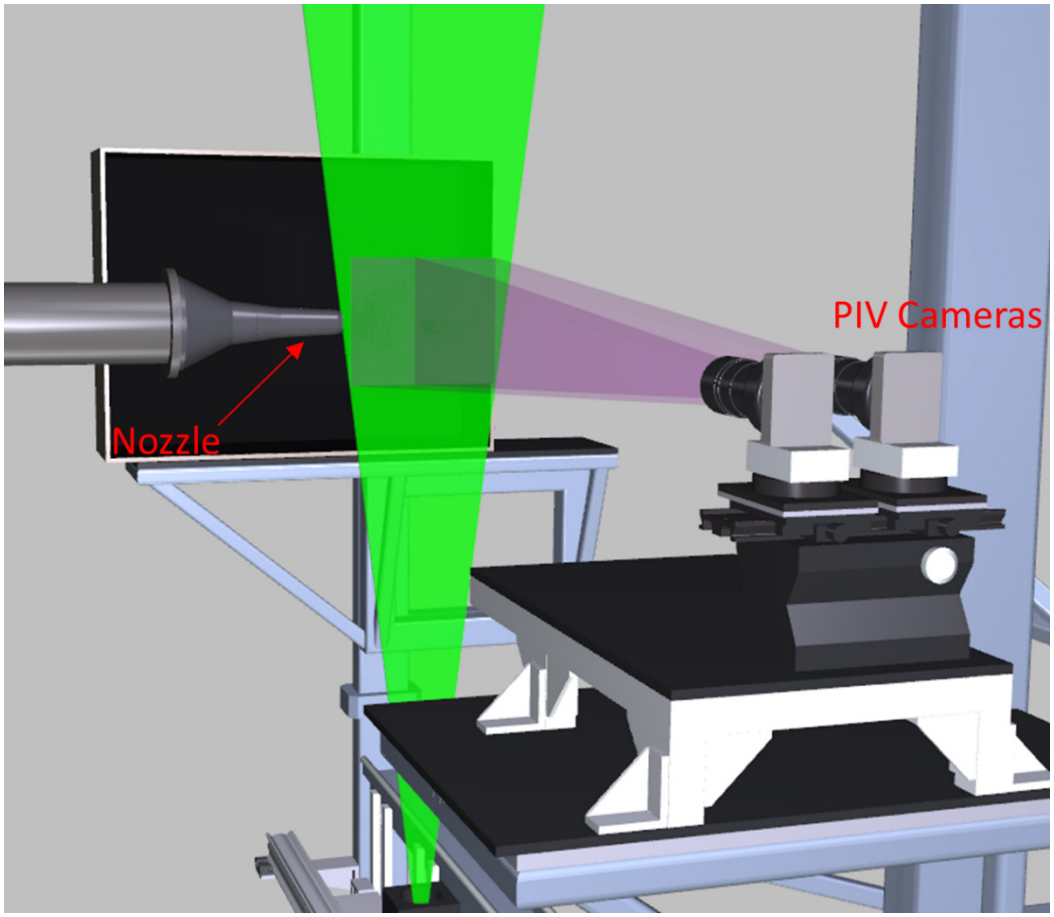

Figure 11.—Streamwise 2-component PIV installation on the SHJAR showing dual side-by-side cameras along with their overlapping fields-of-view and the laser light sheet.

5.3 PIV Vector Processing

Velocity vector maps for each camera were computed from the image pairs using NASA GRC's in-house PIVPROC software (Ref. 27). The software utilizes conventional multi-pass PIV cross-correlation processing algorithms and incorporates error detection based on image correlation signal-to-noise ratio. First-pass interrogation region sizes of 64×64 pixels on 32 pixel centers and final-pass interrogation region sizes of 16×16 pixels on 8 pixel centers were used to process image pairs from the stereo PIV configuration. Symmetric Phase Only Filtering (SPOF) was also employed to reduce the effects of flare light scattered from the nozzle lip, directly behind the measurement planes (Ref. 28). Without the SPOF processing, images with the nozzle illuminated by flare light behind the plane of interest generally produce large regions in and around the potential core flow with invalid vector measurements. The SPOF processing technique was not utilized with the axial-flow measurement planes as the nozzle does not appear in the field of view. Final-pass subregions of 32×32 pixels on 16 pixel centers were used to process the streamwise PIV data. For both the 2C and Stereo PIV setups, sequences of 400 velocity vector maps were acquired at each measurement station. The image sequences were ensemble averaged to provide first- and second-order statistics over the entire measurement plane. Chauvenet's criterion was used to eliminate any outliers in the ensemble averaging process (Ref. 29). The final streamwise 2C PIV velocity vector maps had a spatial resolution of 1.3 mm, while the final cross-stream SPIV velocity vector maps had 1.1 mm spatial resolution. For the 3C SPIV data, the left/right vector maps were processed with an additional in-house code to generate the 3-D vector maps. The 2C streamwise PIV system provides the ω_y component of vorticity and the 3C SPIV data provides the ω_x component of vorticity. The processed PIV data for the streamwise PIV configuration has a full-scale measurement error of 1 percent, while the Cross-stream PIV data have a full-scale measurement error of 2.5 percent.

5.4 Flow Seeding

For any type of PIV measurements, the fluid motion being measured is marked by the use of small particles. These particles must be sufficiently small so they will have minimal or no slip relative to the fluid (so that their motion is the same as the fluid motion). In addition, all of the fluid must be laden with particles at a concentration high enough that sufficient particles (5–10) are found in an interrogation region of the recorded PIV images. In tests using the SHJAR, two fluid streams were being mixed: the heated core nozzle stream and the ambient air. It is also crucial that the flow seeding be fully mixed and dispersed in the flow upstream of the measurement region in order to ensure good-quality PIV images. Finally, the seed particles must not be affected by the high temperatures of the gas.

The hot nozzle flow described above was seeded with a refractory seed material, and the ambient air was seeded using a commercial smoke generator. The refractory seed material used for the heated jet flow was 0.4 μm diameter alumina powder. A dispersion of the alumina seed material in 100 percent ethanol was prepared using a pH stabilization technique (Ref. 30). The alumina/ethanol dispersion was introduced into the flow well upstream of the nozzle using an air-assisted atomizing nozzle. The pH stabilization technique provides highly dispersed, unagglomerated seed particles in the flow. The ambient fluid was seeded with 0.3-μm mineral oil droplets ($\rho_f = 0.84$ gm/cm^3) produced by a commercial 'smoke' generator. A pair of 1-m diameter room circulation fans was used to disperse the concentrated smoke emitted by the smoke generator, providing a low velocity (1 m/s), uniformly seeded ambient air around the research jet.

The flow following fidelity of the particles is important in all PIV studies and especially in a supersonic flow investigation. The relaxation time of the alumina particles was computed to be 1.96 μs using the process outlined in Melling (Ref. 31). Similarly, the relaxation time for the oil droplets used to seed the ambient flow was determined to be 0.1 μs, which is significantly less than the alumina particles. Assuming Stokes drag law for a sphere, a numerical integration was then performed to compute the alumina particle relaxation distance to a step change in velocity across a shock. The distance for the alumina particles to reach 87 percent of the flow velocity was computed, yielding a relaxation distance of 2 mm. The PIV subregions used to process the data were on the order of 1 mm. Hence, the alumina particle relaxation in the jet core is masked by the spatial averaging caused by the subregions. The particle relaxation occurs over 1–2 subregions, which results in minimal smearing of the flow features for the data shown here. However, one of the data sets collected during this test campaign showed possible signs of particle lag, SMC015 at Set Point 1404. This streamwise PIV data set actually suffered from low levels of seed particle concentration in the jet core, which impeded an accurate reconstruction of the sinusoidally varying supersonic flow field in the jet potential core.

6.0 Real-Time Background Oriented Schlieren

Background Oriented Schlieren (BOS) is a widely used technique for measuring density gradients in fluid flows of interest. The attraction of BOS is the simplicity in the setup and data reduction. In this work, two innovations to the BOS technique were employed. First, a GPU based computer was used to acquire and process the BOS image data in real-time, providing a live display of the density gradients in the flow (Refs. 32 and 33). Secondly, an innovative approach for generating the background speckle patterns was employed. The speckle patterns required for the BOS measurement were displayed on a high definition 4 K resolution computer monitor. Use of the 4 K monitor to display the speckle patterns has three distinct advantages: 1) the speckle patterns can be generated on the computer and displayed directly on the monitor without having to physically construct the speckle pattern; 2) the scale of the speckle pattern can be readily changed to optimize the BOS system performance; and 3) the speckle pattern is self-illuminating, which greatly simplifies implementing the technique in confined environments, or where illumination of a static speckle pattern may be difficult or problematic. A 2.4×2 K pixel, GigE interface camera was used to image the speckle pattern displayed on a 1092 mm (43 in.) diagonal 4 K resolution monitor. The camera was mounted on a shelf on the large traverse system and the monitor was mounted directly across from the camera on a separate shelf, as shown in Figure 12. The size and density of the speckle pattern selected for display on the 4 K monitor was determined before the test using an optimization software package. The configured Real-Time BOS system runs through an optimization algorithm, which cycles through a range of speckle patterns displayed on the 4 K monitor while monitoring the background noise in the processed BOS images. The optimization process yields the maximum sensitivity in the configured BOS system. The selected speckle pattern contained a continuum of gray scale speckles, not a binary pattern. The processed density gradient maps were processed and displayed at the maximum 12 Hz frame rate of the 5 MP GigE camera.

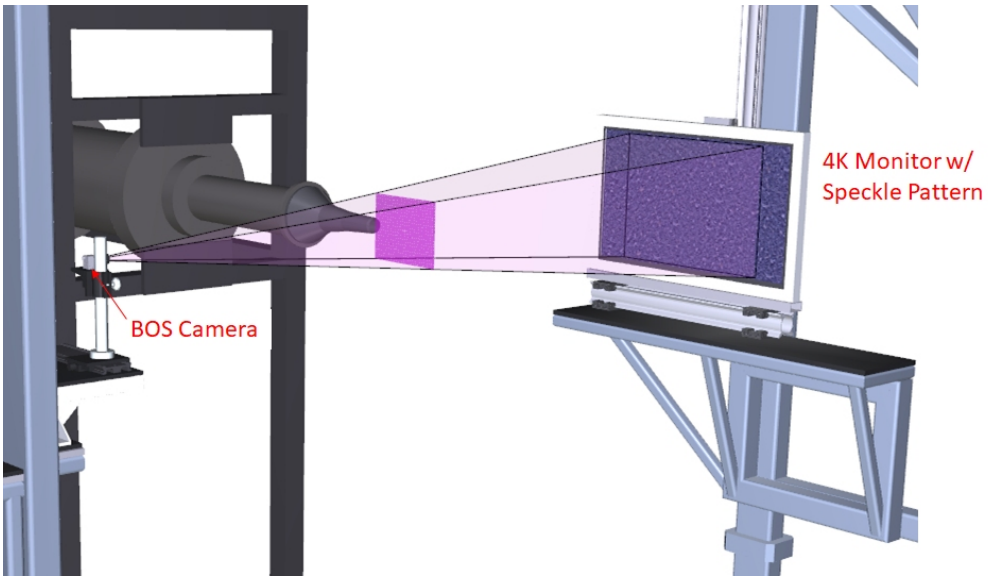

Figure 12.—Background Oriented Schlieren (BOS) system installation in the SHJAR. The field of view of the BOS system at the centerline of the jet is indicated by the magenta rectangle.

7.0 Probe Measurements

The large traverse system in the SHJAR also contains plume survey rakes, which consist of a pair of vertical airfoil shapes each containing a linear array of 56 pressure probes or temperature probes positioned on 6.35 mm centers as shown in the CAD rendering in Figure 13(a). The vertical airfoils are laterally offset from one another by 75 mm to avoid contaminating each other's measurement of the flow. The probes protrude approximately 16 mm from the airfoil body. The pressure probes are stainless tubes connected to a bank of static pressure sensors. The total temperature probes are a shielded and vented design using 2.3 mm tubes with 1.57 mm Type N exposed-ball thermocouples mounted inside. The tubes have cross-drilled holes in them equal to approximately ½ the area of the open end of the tube in order to allow air to flow through the tube providing continuous flow of air surrounding the thermocouple, yet measuring the total (stagnation) temperature. The vertical airfoils were mounted on a spanwise translation stage, enabling profiling of the nozzle flow. Full mapping of the nozzle flow was achieved by combining the large traverse's capability to set the axial station along with the plume survey rakes spanwise positioning capability. The rakes were vertically positioned so that one of the 56 probes was located on the vertical centerline of the nozzle. Although 56 measurement points are available, for this test the vertical centerline probe information was of most interest. The probe rakes were traversed axially from 0.5 nozzle diameters (25.4 mm) to 24 diameters (1219.2 mm) downstream.

Accurately estimating the Mach number using pitot pressure probes in flows with even weak oblique shock waves is challenging without knowledge of the local static pressure. Figure 13(b) shows a photograph of the bow shocks forming upstream of the rake near the nozzle exit and an expanded schematic of a bow shock formed upstream of a pitot probe in a supersonic flow. In the schematic of Figure 13(b), P_1 is the local static pressure at the probe, P_∞ is the far field ambient pressure, P_{t1} is the total static pressure upstream of the shock and P_{t2} is the total static pressure downstream of the shock. As an example, consider a jet flow with weak shock waves operating at a pressure ratio that would yield a Mach number of 2.00 in the jet plume. Assume there are weak compression and expansion waves with negligible total pressure losses in the potential core region of the jet. Consider the scenario where at a fixed position, the actual Mach number at a point is 1.90. Using a specific heat ratio, $\gamma = 1.4$, the pitot

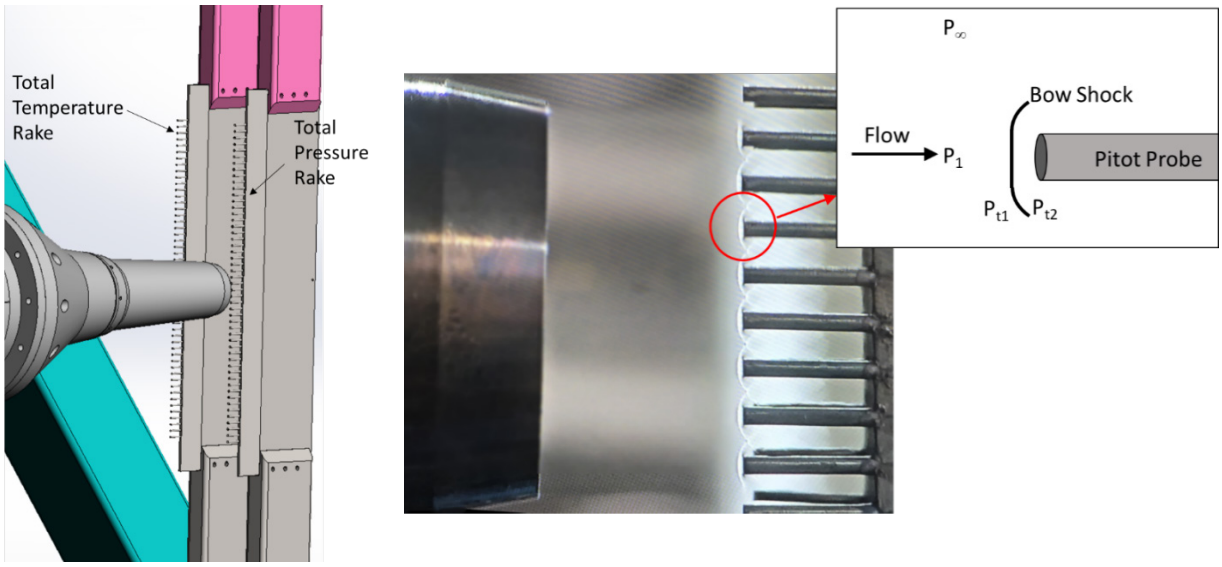

(a) (b)

Figure 13.—(a) CAD rendering of the pressure and temperature plume survey rake installed in the SHJAR; (b) Picture of bow shocks upstream of the rake and schematic blow up of bow shock upstream of single pitot probe.

pressure, P_{t2}, which is the measurement of total pressure after a normal shock, is 1.065 times larger than P_{t2} at Mach 2.00. However, the local static pressure, P_1 is 1.168 times larger than the far field static pressure, equal to the static pressure when the local Mach number is exactly 2.00. The term P_1/P_{t2}, is 1.097 times larger at Mach 1.90 than Mach 2.00. However, because the local static pressure is not traditionally measured at exactly the same point, and the far field ambient pressure, P_1 is used in place of the actual local static pressure, the term P_1/P_{t2} is incorrectly calculated to be 1.065 times smaller, which corresponds to a Mach 2.07 flow. The converse would be the case for locations in the flow where the Mach number was actually higher than the perfectly expanded Mach number, and the predicted Mach number would be incorrectly computed to be lower than the perfectly expanded Mach number.

In order to calculate the local Mach number in the current experiments, a procedure was developed where it was assumed that for the first 60 percent of the potential core, the static pressure cannot be determined. Instead, the local jet stagnation pressure is assumed to be equal to the supply stagnation pressure with no losses due to the weak compression and expansion process in the potential core. Hence, the ratio P_{t2}/P_{t1} is used to calculate the local Mach number. Starting at end of the potential core, the static pressure is assumed to have adjusted to the measured ambient value, and that P_1/P_{t2} can be used to accurately determine the Mach number. Between these two points in the potential core, both techniques are still employed despite being outside the regions where the two assumptions are strictly valid. In this overlap region, a linear interpolation is used for the Mach number and static pressure in order to compute the local stagnation pressure.

The algorithm developed to process the pressure probe data into Mach number described above is unique compared to previous published works on utilizing probe data in supersonic flows. As an example, a RANS solution for a Mach 2 nozzle flow was computed, where the centerline Mach number, shown as a solid line in Figure 14, depicts the multiple weak expansions and compressions within the potential core. The local values of P_t were then used to reconstruct the Mach number along the centerline using the traditional approach of Seiner et al. (Ref. 1) and also the algorithm described above. The Mach number profile computed via the traditional approach, plotted as dash-dot line in Figure 14 using the assumption $P_1 = P_\infty$, is clearly out of phase with the true Mach number profile down the jet centerline. However, the

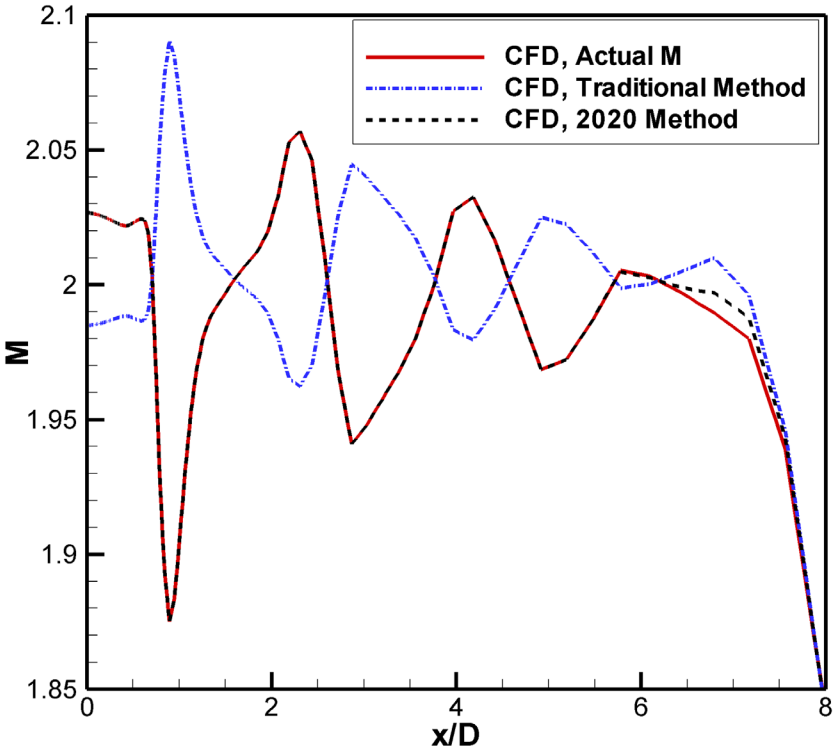

Figure 14.—Comparison of the centerline Mach number computed using the traditional approach of Seiner, et al. (Ref. 1) compared with the new algorithm outlined here.

Mach number profile computed using the algorithm described above yields the dashed line in Figure 14, which exactly overlaps the actual Mach number profile except for a short region at the end of the potential core, $6 < x/D < 8$, where the computed Mach number is slightly above the actual value. Hence, the algorithm described herein is the preferred approach for accurately extracting Mach number data from the pressure probe measurements.

The stagnation temperature-probe measurements required calibration in order to yield accurate estimates of the total temperature. Albertson (Ref. 4) discussed that deviations between actual and measured stagnation temperatures for shielded probes as used in this experiment are due to a combination of conduction, convection, and radiation effects. The method used to construct a calibration for the total temperatures measured in this experiment is as follows: The difference between the measured plenum stagnation temperature and stagnation temperature measured in the jet potential core was tabulated for every operating point in the test matrix. A third-order polynomial was used to fit this difference, or error, as a function of jet plenum stagnation temperature minus ambient static temperature, $T_{t,Plenum} - T_{\infty}$. Interestingly, the resulting curve fit was nearly linear. This correction was used for temperatures measured in the potential core. For locations in the potential core and especially near the nozzle exit, the thin shear layer and demarcation between the heated portion of the temperature probe rake and the unheated portion was believed to result in significant conduction heat loss from the region of the rake and probes measuring the highest temperatures. Far downstream of the potential core where the jet had mixed and spread outward, the conduction losses were significantly lower, and no correction was required. Analogous to the interpolation used for the stagnation pressure probe, the stagnation temperature correction was interpolated between the corrected and uncorrected value using a quadratic function. At each point, the corrected stagnation temperature and derived Mach number were used to calculate the static temperature, speed of sound, and local jet velocity. The local specific heat ratio γ along the jet

centerline was also computed as a function of the calculated temperature. While γ did not vary significantly for the temperatures under investigation, an iterative procedure was used to obtain a converged set of these flow properties. It should also be noted that while the hydrogen burner used to heat the nozzle flow produced vitiated air with water vapor in the combustion products, the effect of water vapor on γ was considered to be negligible, so the temperature variation with γ used the clean air formulation (Eqn. 180) from Reference 5.

Based on the configuration of the SHJAR facility data acquisition systems, the error in the measured pressures was ±0.1 psi and the error from the thermocouples was ±3 K. Hence, the errors in the thermocouple measurements of T_t are ±3 K. As described above, the probe measured values of P_t and T_t were used to estimate the velocity. Due to the complicated and iterative process for extracting the velocity data from the probe measurements, a direct error analysis was not feasible. Instead, a perturbation analysis was performed using the known errors in the probe measurements to examine the propagation of those errors into the velocity estimates. The errors were first examined for Set Point 2001, where the jet exit temperature was matched to the ambient air temperature. Within the potential core, the major error source was the thermocouple error, which yielded errors as high as 2.3 m/s, or approximately 0.35 percent of the jet exit velocity. At the end of the surveys near x/D = 40, the pressure readings yielded the larger source of error, but the overall error was still on the order of 0.5 percent of U_j. The error was lowest near the end of the potential core where the transition from a static pressure based on the supply pressure to one based on the ambient pressure was employed, apparently, without significant effect in the estimates. For the heated flow cases, the use of the corrected T_t values yielded similar error levels as the temperature matched case. If temperatures had not been corrected for installation effects, then the maximum errors in the velocity estimates would have been on the order of 2 percent of U_j.

8.0 Baseline CFD Analysis

The focus of this paper is on the experimental measurements that were made in order to evaluate and improve CFD and not an extensive CFD investigation. Hence, in order to establish the current state-of-practice for such an experimental configuration, a set of CFD runs were obtained using standard Reynolds-averaged Navier-Stokes (RANS) modeling. CFD simulations of the experimental configuration were run using the Wind-US CFD code (Ref. 34), a general purpose CFD solver used extensively at NASA GRC for inlet, nozzle, and other propulsion flow simulations. The simulations were run in axisymmetric Reynolds-averaged Navier-Stokes (RANS) mode, using the Menter SST k-ω shear stress transport (SST) model (Refs. 35 and 36). The turbulent Prandtl number, Pr_t, was set to 0.7 for these cases. The ratio of specific heats was set to 1.4 for all cases considered herein. A structured computational grid having 146,455 points across three zones was constructed using the Pointwise software (Ref. 37). Grids were packed to solid surfaces such that the first point off the wall was within the laminar sublayer. The nozzle was modeled from slightly upstream of the junction with the facility supply pipe to allow a boundary layer to grow inside the nozzle. The wall surface was set to an adiabatic no-slip surface. In the jet plume zone, the computational grid extended 40 diameters axially and 20 diameters radially. The grid was also concentrated axially and radially in the initial part of the jet plume region to resolve the jet mixing and weak expansions and compressions in the jet potential core. A freestream Mach number of 0.02 was set to prevent any convergence difficulties with compressible flow solvers. Previous simulations of jets exhausting into quiescent ambient (Ref. 38) indicate that a freestream flow of this speed would yield jet decay very similar to quiescent air.

9.0 Results and Discussion

The set of operating points for which comprehensive data was collected using all of the measurement techniques, is shown in Table 2. The Set Point numbers in Table 2 correspond to the nozzle that was used in the testing; i.e., 140* corresponds to the Mach 1.36 (perfectly expanded) nozzle denoted as SMC015, 166* corresponds to the Mach 1.63 nozzle denoted as SMC017, and 200* corresponds to the Mach 2.0 nozzle denoted SMC020. In addition to the Mach number of the air supply if perfectly expanded, the set point designation number defines the difference between the jet static temperature at the jet exit and the ambient static temperature, ΔT. All of the values in Table 2 represent the ideal planned set point conditions and were computed using the gas constant R for clean air and $\gamma = 1.4$. The actual operating conditions at each set point for each different type of data being collected varied slightly due to: variations in the water content in the combusted air; day-to-day variations in the ambient temperature; and the fact that the data were collected on different days. One final note, there are inconsistencies in the Set Point naming since additional set points were added to the matrix while the test was underway.

9.1 Pressure and Temperature Probe Results

Total pressure and temperature data were acquired using the probe rakes as described previously. The measured pressures were used to derive the Mach number at each measurement station, and then the corrected stagnation temperature with Mach number was used to calculate a static temperature, speed of sound, and ultimately, streamwise (or axial) velocity. A comparison of centerline velocity and total temperature profiles for the Mach 2 jet is shown in Figure 15. The normalized velocities are plotted in Figure 15(a), where the Seiner et al. (Ref. 1) data are plotted as solid lines and the THX5 probe data are plotted as dashed lines. The SHJAR facility was only capable of matching three of Seiner's set points: 2001, 2002, and 2004. The fourth case, Set Point 2003, with $\Delta T = 233$ K represented the highest operating stagnation temperature for the SHJAR. Due to the inability to obtain a perfectly matched jet, the THX5 probe data exhibit some oscillations in the potential core due to the non-shock free flow of the jet. Seiner's data shows significantly smaller oscillations in velocity within the jet potential core possibly due to his assumption of $P_1 = P_\infty$ as discussed in Section 7.0. Generally, the THX5 probe data exhibit a

TABLE 2.—OPERATING SET POINTS WITH OPERATING CONDITIONS

Nozzle	Set Point	M_{Ideal}	ΔT [K]	$T_{s,Ideal}$ [K]	$T_{T,Plenum}$ [K]	$P_{T,Plenum}$ [kPa]	ρ_{Ideal}[kg/m^3]	U_j [m/s]
SMC020	2001	2	0	293	520	776.85	1.1981	679
SMC020	2002	2	133	406	760	776.85	0.8196	833
SMC020	2003	2	233	509	940	776.85	0.6626	932
SMC020	2004	2	-128	165	289	776.85	2.1568	512
SMC017	1661	1.63	0	285	442	441.24	1.1981	544
SMC017	1665	1.63	133	408	657	441.24	0.8065	669
SMC017	1662	1.63	233	508	799	441.24	0.6626	745
SMC017	1664	1.36	233	514	715	298.75	0.6626	580
SMC015	1401	1.36	0	278	396	298.75	1.1981	457
SMC015	1405	1.36	133	418	578	298.75	0.8196	549
SMC015	1402	1.36	233	516	715	298.75	0.6626	605
SMC015	1404	1.63	233	510	799	441.24	0.6626	721
SMC015	1403	1.36	333	618	852	298.75	0.5561	662

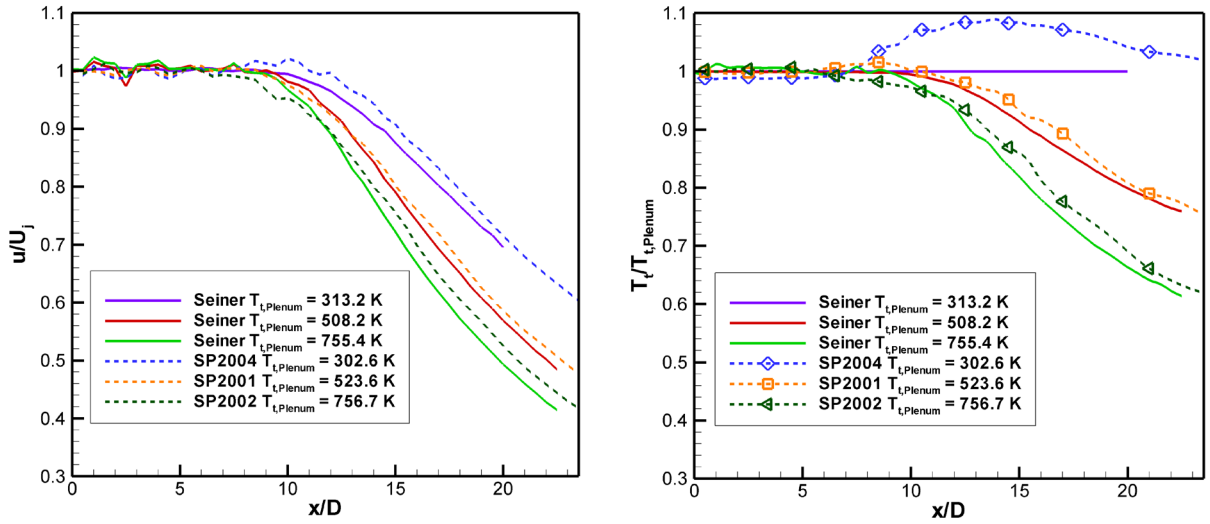

(a) (b)

Figure 15.—Comparison of Seiner data to THX5 probe data: (a) Normalized velocity; (b) Normalized total temperature.

slightly slower decay rate in velocity compared to the Seiner data. However, the overall agreement between the two sets of probe data taken three decades apart is very close. The largest deviation between the two sets of measurements is in the intermediate region where there was no reliable pressure ratio to use for the estimation of the Mach number. Figure 15(b) compares the THX5 corrected, normalized total temperature profiles to those of Seiner. Again, the solid lines are the Seiner data and the dashed lines are the THX5 data covering set points 2001, 2002, and 2004. Note that for Set Point 2004, Seiner et al. (Ref. 1) indicated that the nozzle flow was very slightly heated to a stagnation temperature of 313 K in their experiments. The data file for this case shows the stagnation temperature to be constant for all axial locations, even beyond the end of the potential core. It is most likely that the stagnation temperature was not measured for this case in their experiments. The rise in the THX5 normalized total temperature measurements for SP2004 past the end of the potential core is currently unknown, but can possibly be due to the heating observed across the shear layer for the temperature matched $\Delta T = 0$ cases, which will be discussed later in Section 9.6. The peak in the SP2004 $T_t/T_{t,Plenum}$ data in Figure 15(b) is also the main source for $u/U_j > 1$ past the end of the potential core in Figure 15(a). The data sets at 500 K (SP2001) agree very well within the potential core, with a slight difference beyond the potential core. A similar trend is observed at the highest temperature comparison at $T_{t,Plenum} = 750$ K (SP2002), where the THX5 data decays slower than the Seiner data. The THX5 temperature measurements are likely to have the higher error of the two data sets for the elevated temperature set points. The large rake with 56 separate probes used for temperature measurements may have advantages in test programs involving other larger nozzles tested in the NASA Glenn Research Center Aero-Acoustic Propulsion Laboratory (AAPL) in terms of the number of points that can be simultaneously measured. However, the large rake and supporting hardware most likely led to heat transfer and resultant larger measurement uncertainties than those experienced in the Seiner experiments where only a single stagnation temperature probe was used.

9.2 Background Oriented Schlieren Results

The SMC nozzles were designed using "idealized" perfectly expanded conditions, yet when installed in the SHJAR, they still yielded weak shocks. The real-time BOS system, with the live display, provided a means for adjusting the rig operating pressure and jet exit temperature to yield a nearly shock free potential core flow. Small adjustments (up to approximately 10 kPa (~1 percent) for the Mach 2 case) to the rig set point pressure were required to achieve a shock free exit. BOS and probe measurements of the jet plume flow were acquired before Raman or PIV measurements were collected. The processed BOS measurements were used to determine the locations of the Raman measurement points across the shear layer. Because the number of Raman temperature measurement locations was time-limited, these BOS images were very helpful in setting and optimizing these locations. Examples of the BOS results are shown in Figure 16 for SMC015 at both Set Point 1402 ($\Delta T = 233$ K) and Set Point 1401($\Delta T = 0$ K) as color contour maps of density gradient magnitude. The density gradient magnitude is used since it incorporates both the x- and y-components of the measured density gradients and best illustrates the series of weak compressions and expansions in the potential core. For the 1402 case shown in Figure 16(a), the highest gradients in density are across the shear layer near the nozzle exit. Across the potential core the density gradients are relatively flat as denoted by the blue region. The density gradient map also shows that the matched pressure at the nozzle exit still results in a series of weak compressions and expansions. These weak compressions and expansions are enclosed within the top and bottom shear layers in the density gradient maps, denoted initially by the bright red regions, which thicken and fade to green with increasing axial distance. For the Set Point 1401 result in Figure 16(b), the processed BOS data again reveals a series of weak compressions and expansions in the jet plume. The scale range of the density gradient fluctuations at Set Point 1401 is much smaller than the one used in Figure 16(a) for Set Point 1402, due to the small-scale fluctuations when the temperature gradient between the jet core and the ambient is set to 0. An interesting feature is observed at Set Point 1401 and in all of the $\Delta T = 0$ cases; there is a region of minimal density gradient magnitude in the middle of the shear layer, as denoted by the dark blue regions running down the center of the shear layer. Actually, the density gradient magnitude plot is masking the sign of the density gradient across the shear layer. Figure 16(c) shows only the y-component of the density gradient map for Set Point 1401, which illustrates the change in sign in the density gradient across the shear layer. The blue region running down the center of the shear layer in the density gradient magnitude plot in Figure 16(b) actually delineates the region where the density gradient changes sign, and therefore defines the minima in density across the shear layer. The shear layer is defined as the region where the high-speed jet flow mixes with the quiescent ambient air. For Set Point 1401, where the temperature of the jet core flow is matched to the ambient, the mixing of the high-speed jet flow with the quiescent ambient air actually results in a measurable increase in the local gas temperature. The thermal dissipation due to mixing is faster than the thermal diffusion, resulting in the localized increase in the gas temperature along the entire length of the shear layer, yielding the observed low-density trough in the BOS data.

9.3 General Raman Temperature and Density Results

Temperature data were acquired over a wide range of flow temperatures and Mach numbers as listed in Table 2. In this paper, results for seven of these conditions are presented: 1) SMC015 at Set Point 1402 (M1.36, $\Delta T = 233$ K); 2) SMC015 at Set Point 1401 (M1.36 $\Delta T = 0$ K); 3) SMC017 at Set Point 1664 (M1.36, $\Delta T = 233$ K); and 4) SMC020 at Set Points 2001, 2002, 2003, 2004. Figure 17 illustrates a typical Raman temperature measurement grid, which is actually a combination of three separate profiles: centerline (r/D = 0), lip-line (r/D = 0.5) and radial profiles at 9 axial stations. A thin line is drawn

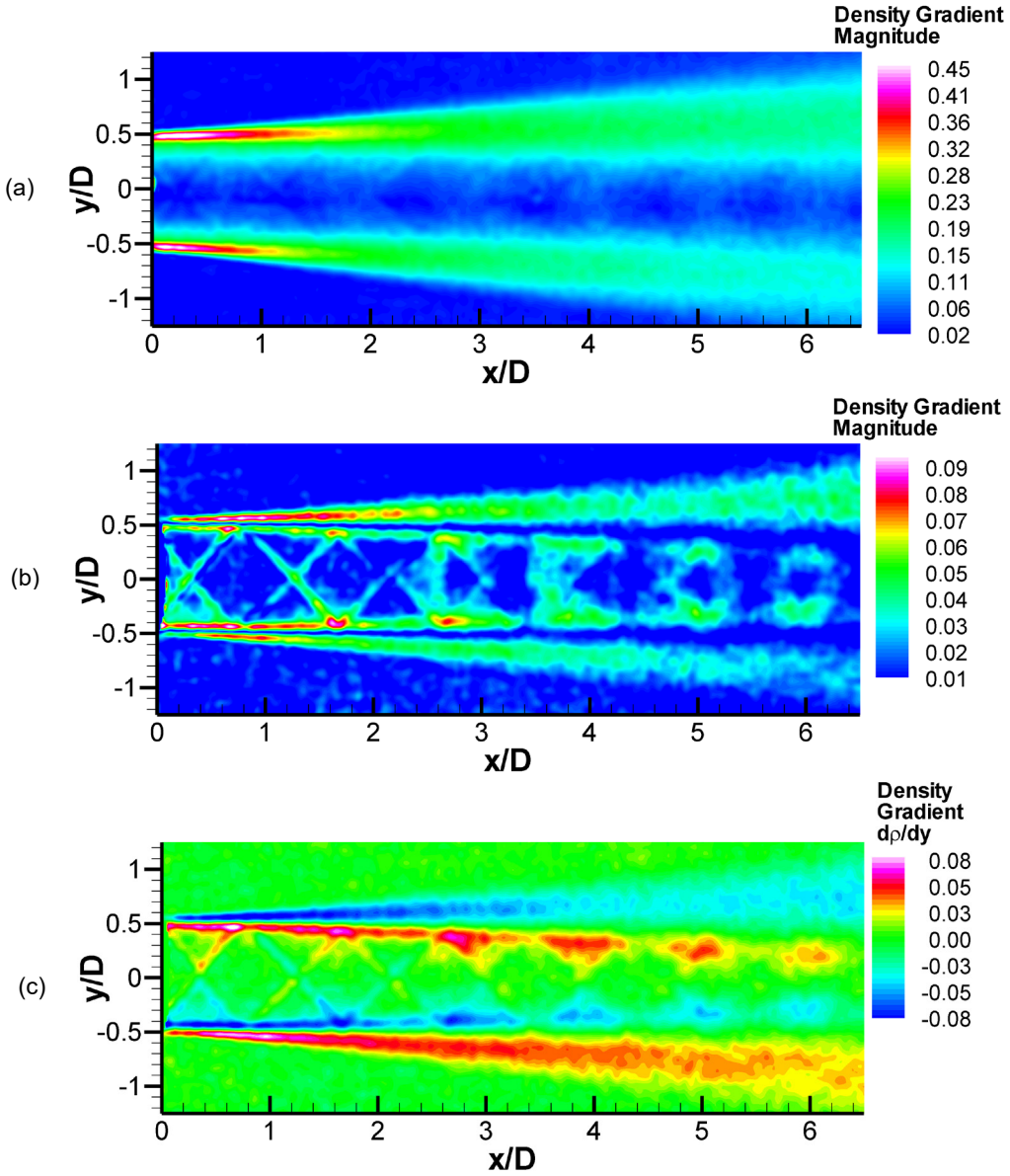

Figure 16.—BOS density gradient maps for SMC015: (a) Density gradient magnitude at Set Point 1402; (b) Density gradient magnitude at Set Point 1401; (c) y-component of the density gradient at Set Point 1401.

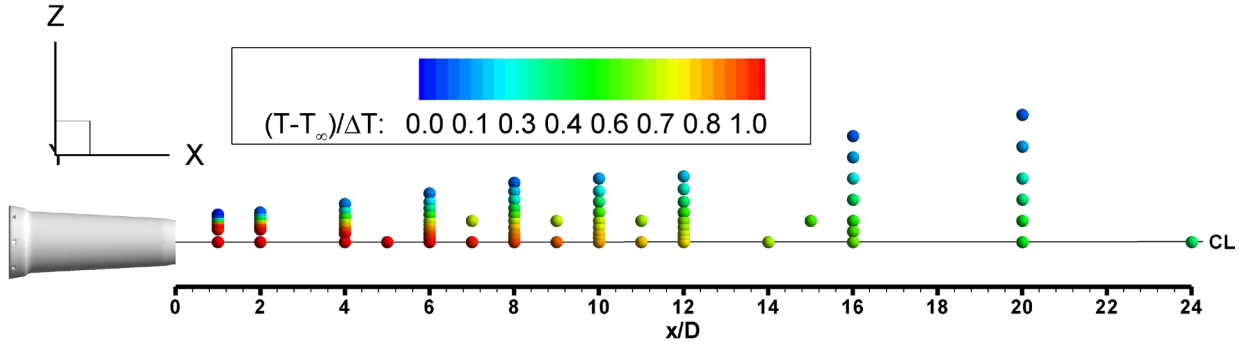

Figure 17.—Nominal measurement grid and an example of Raman measured temperatures for SMC015 at Set Point 1402.

depicting the nozzle centerline. The symbols in the scatter plot are colored by their nondimensional temperature. The radial profiles overlapped both the centerline and lip-line profiles. On some run days the lip-line profiles were not acquired – but could be reconstructed from the radial profiles. Comparison of the lip-line profile reconstructed from the radial profiles to actual lip-line profiles show excellent agreement. An ambient temperature point was acquired prior to the start of each run day using the Raman measurement system. These ambient temperatures and their rms temperature variations provide a check on the performance of the Raman measurements in the jet flow facility.

Nominally, only 120 Raman measurement points can be collected in a single run day in the SHJAR. The BOS measurements provided a clear picture of the extent of the jet shear layer and facilitated the optimization of the Raman radial profile measurement grids. The measurement grids for each Set Point are in general not identical, depending on the growth of the shear layer and length of the potential core. Raman centerline measurements were acquired at 15 axial locations (x/D = 1, 2, 4, 5, 6, 7, 8, 9, 10, 11, 12, 14, 16, 20, and 24) for all set points except Set Point 1405, where only 14 axial stations were acquired on the centerline. The lip-line profiles were acquired at 12 axial stations (x/D = 1, 2, 4, 6, 7, 8, 9, 10, 11, 12, 15, and 20). Radial profiles were acquired at axial stations of x/D = 1, 2, 4, 6, 8, 10, 12, 16, and 20. The spacing of measurement points at each axial station were adjusted to cover the thickness of the jet shear layer. Typically, 10 points were acquired in each radial profile. After the unexpected drop in the density gradient was observed in the BOS data, additional points were added to the $\Delta T = 0$ Set Point radial surveys. At the beginning of a run day, spectra were recorded to provide a background spectra for baseline removal. At each measurement station, 1000 single shot spectra were recorded. The data were processed as previously described, ensemble averaged, and stored in Tecplot compatible file formats.

When collecting the Raman scattered light, an edge filter is used to block the Rayleigh scattered light, which occurs at the laser-line wavelength of 532 nm. Some Rayleigh light may still leak through the filter, depending on the intensity of the light. Typically, there are no particles in the flow when acquiring the Raman data. When particles and/or condensation are present in the air, they scatter light at the laser line wavelength. The particle scattered light is orders of magnitude brighter than the Rayleigh light scattered by molecules. Hence, particles in the flow can be problematic for processing the Raman spectra. In cases where there is some particle contamination in the flow, additional checks on the Raman spectra signal amplitude, especially around the laser line wavelength, are used to remove any particle laden spectra from the ensemble of measurements used to compute the mean and rms values. In this experiment, even the $\Delta T = 0$ case resulted in some condensation in the jet core, yet Raman temperature measurements were still possible under these conditions. More aggressive filtering was applied to ensure that no particle contaminated spectra were being used to compute the mean and rms quantities, fortunately; the extra filtering had no impact on the mean and rms temperature estimates from the Raman spectra, confirming that the Raman temperature estimates were unaffected by the particle scattered light. Conversely, the density estimates are directly dependent on the scattered light signal level. When processing the Raman spectra to estimate density, more aggressive filtering was required, yielding only 700 spectra in the ensembles for estimating the density. This was done as a precaution against biasing the density estimates. Reducing the number of good spectra below 700 had no noticeable impact on the computed density properties.

9.4 General PIV Velocity Results

Both streamwise and cross-stream PIV data were collected across all of the Set Points listed in Table 2. Cross-stream PIV data were collected at many of the same axial locations as the Raman temperature measurements, x/D = 1, 2, 4, 6, 8, 10, 12, 16, and 20. The cross-stream PIV data at 9 planes were processed and merged into a single block of data and stored in Tecplot compatible file format. As mentioned in the data processing section, obtaining cross-plane vector maps without contamination from the model in the background is very difficult. The issue is exacerbated by the alumina seed material, which coats the inside surface of the nozzle over time making it white and therefore brighter in the background of the illuminated PIV measurement planes. The flare light from the nozzle in the background results in regions of low signal to noise in the images, which causes spurious vectors in the processed vector maps. The streamwise PIV dual camera had a field of view of 355×300 mm and was traversed in four 300 mm increments to map the centerline plane of the nozzle jet plume. Figure 18 shows color contours of the normalized axial velocity u/U_j for SMC015 at Setpoint 1402 from both the cross-stream PIV planes and streamwise PIV centerline plane. The cross-stream planes match up well with the centerline plane. Residual contamination from flare light scattered off of the model is observed in the cross-stream planes near the nozzle exit. The bright edge of the nozzle yields crescent shaped regions of spurious vectors in the processed vector maps for x/D < 4. For the low temperature cases, some condensation was observed in the jet plume. The condensation actually occurs in the shear layer where the moist ambient air mixes with the cold jet potential core air. The condensation reaches a maximum at the end of the potential core where the conical shear layer eventually collapses. Although present for the ΔT = 0 cases, the condensation did not adversely impact the PIV measurements. However, for the ΔT = –128 K case, condensation was significant and limited the useful region of the PIV data to the length of the potential core.

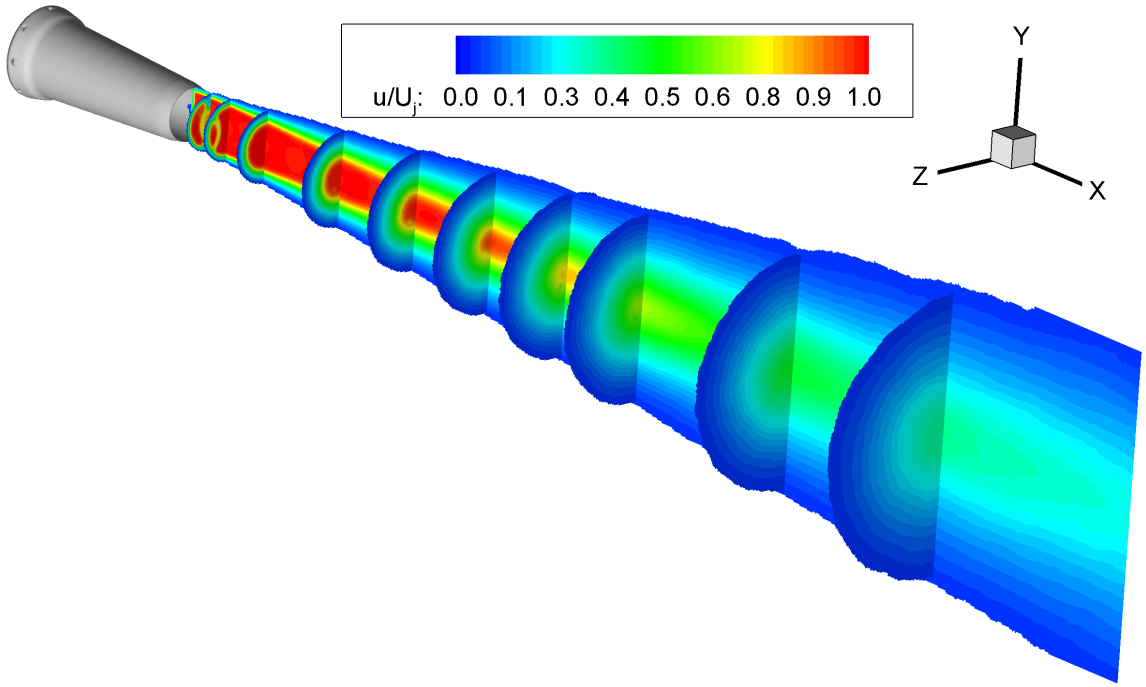

Figure 18.—Color contour plot of normalized axial velocity from both cross-stream and streamwise PIV measurements for SMC015 at Set Point 1402.

Figure 19 illustrates the breadth of the data sets collected, where the various 2nd order statistics computed from the streamwise PIV data are shown for Set Point 1402. The mean axial velocity component is shown along with the two normal stresses and the primary shear stress. All of the turbulent stresses are normalized by the square of the jet exit velocity for this case: 615 m/s. The nonzero patches in the top of $v'v'/U_j^2$ are noise artifacts from image bleed through on the frame-straddling setting on the PIV camera in the regions where the four axial stations of processed vector maps are seamed together. These noise artifacts are to be ignored.

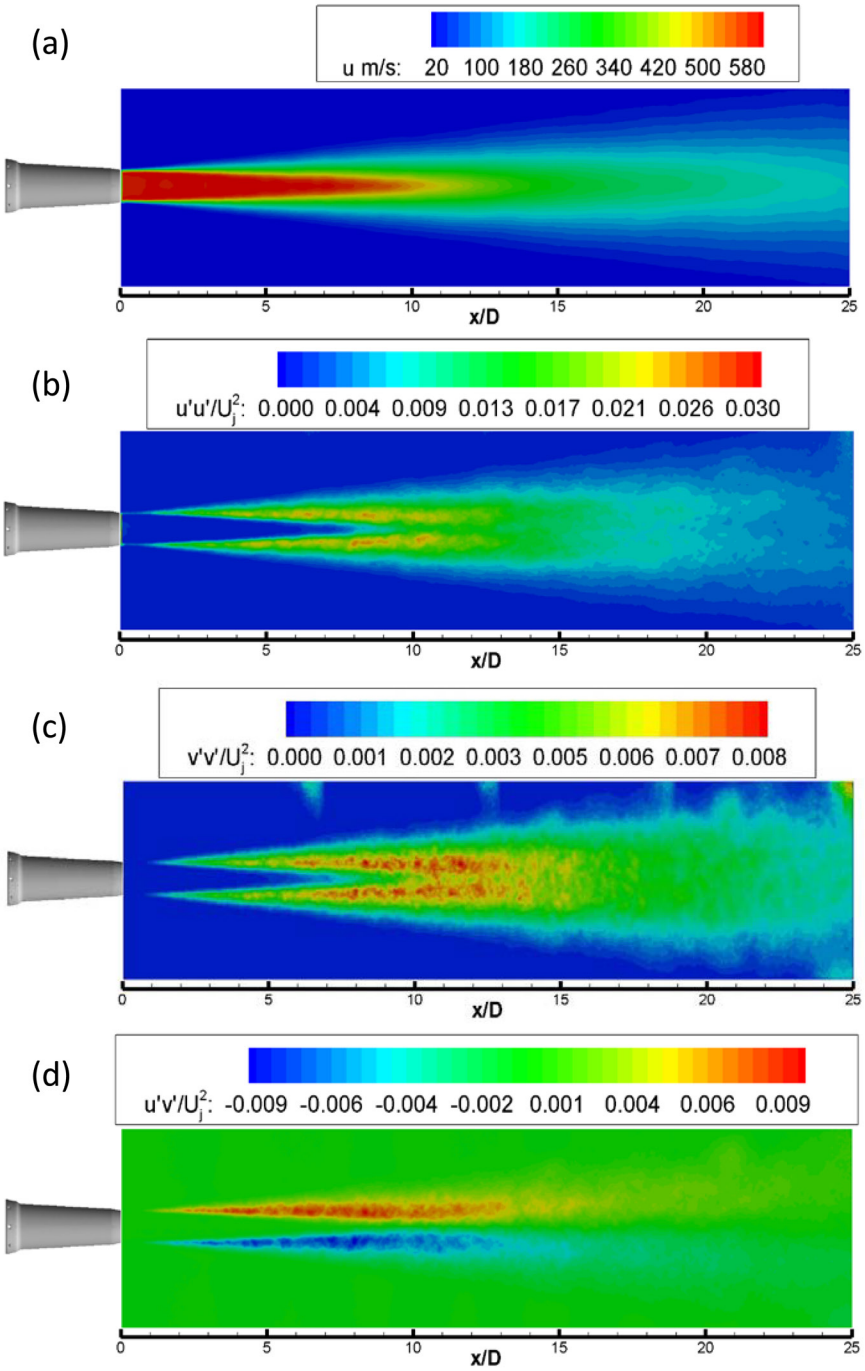

Figure 19.—Streamwise PIV for Set Point 1402: (a) u [m/s]; (b) $u'u'/U_j^2$; (c) $v'v'/U_j^2$; (d) $u'v'/U_j^2$.

9.5 SMC015 Set Point 1402 PIV and Raman Results

The streamwise PIV data were acquired in the x-y plane as shown in Figure 17, while the Raman data were collected in the x-z plane as depicted in Figure 18. From this point forward, all radial profiles are plotted as r/D where no distinction is made between z/D or y/D. The Raman data yield both the mean and rms fluctuations in the gas temperature. The Raman temperatures are nondimensionalized using the computed static temperature at the jet exit and the ambient temperature $(T-T_\infty)/(T_{s,\,Ideal}-T_\infty)$. The streamwise PIV mean and rms velocities are normalized by the jet exit velocity U_j. The centerline (r/D = 0) nondimensional mean and rms temperatures and velocities are plotted in Figure 20(a), where the Raman data are shown with both symbols and lines. The limited spatial resolution of the Raman temperature measurement grid was unable to resolve the probable small-temperature oscillations within the potential core. For x/D >10 the nondimensional temperature decays more slowly than the normalized velocity. The nondimensional rms temperatures and velocities are generally low inside the potential core of the jet (x/D < 8) and then increase beyond the end of the potential core as the hot, high-speed core flow mixes with the cooler, quiescent ambient air. The lip-line (r/D = 0.5) nondimensional mean and rms temperatures and velocities are plotted in Figure 20(b), where the Raman data are shown again with both symbols and lines. The lip-line nondimensional mean temperature measurements have a similar shape to the velocity measurements, although the magnitudes of the nondimensional quantities are rather different. The nondimensional rms temperatures and velocities exhibit similar shape and magnitude, exhibiting an initial rise followed by a generally monotonic decay downstream.

The streamwise normalized PIV velocity data for SMC015 at Set Point 1402 (ΔT = 233 K) are plotted as line profiles along the nozzle centerline (r/D = 0) in Figure 21(a). For comparison, a RANS solution for the identical flow case is also shown in the plot. The PIV and RANS data agree very well along the centerline within the potential core of the jet, matching both the length, shape and location of the weak shock structures. The RANS solution has an abrupt drop at the end of the potential core and predicts a faster decay of the velocity beyond the potential core (x/D > 8) which is a known issue for RANS models in computing compressible jet flows. Figure 21(b) shows a comparison of the PIV data versus the CFD prediction on the nozzle lip-line (r/D = 0.5). The lip-line profiles have nearly identical shape, but the magnitude of the velocities differ by approximately 10 percent. Radial profiles of the RANS solution (dashed lines) are plotted against PIV data (solid lines) in Figure 21(c), where only a subset of the total

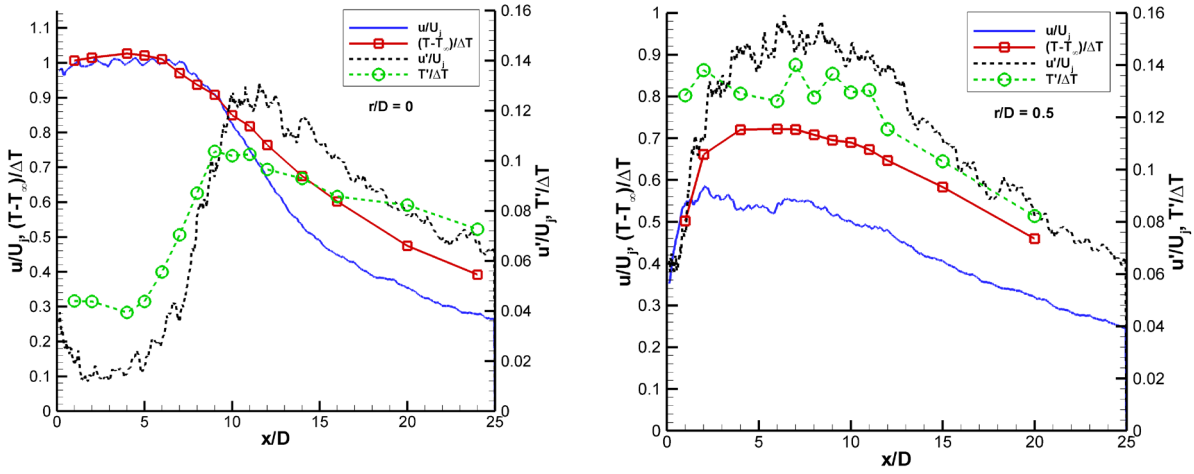

Figure 20.—SMC015_1402 Nondimensional mean and rms temperature and velocity profiles on (a) Centerline (r/D = 0); (b) Lip-line (r/D = 0.5).

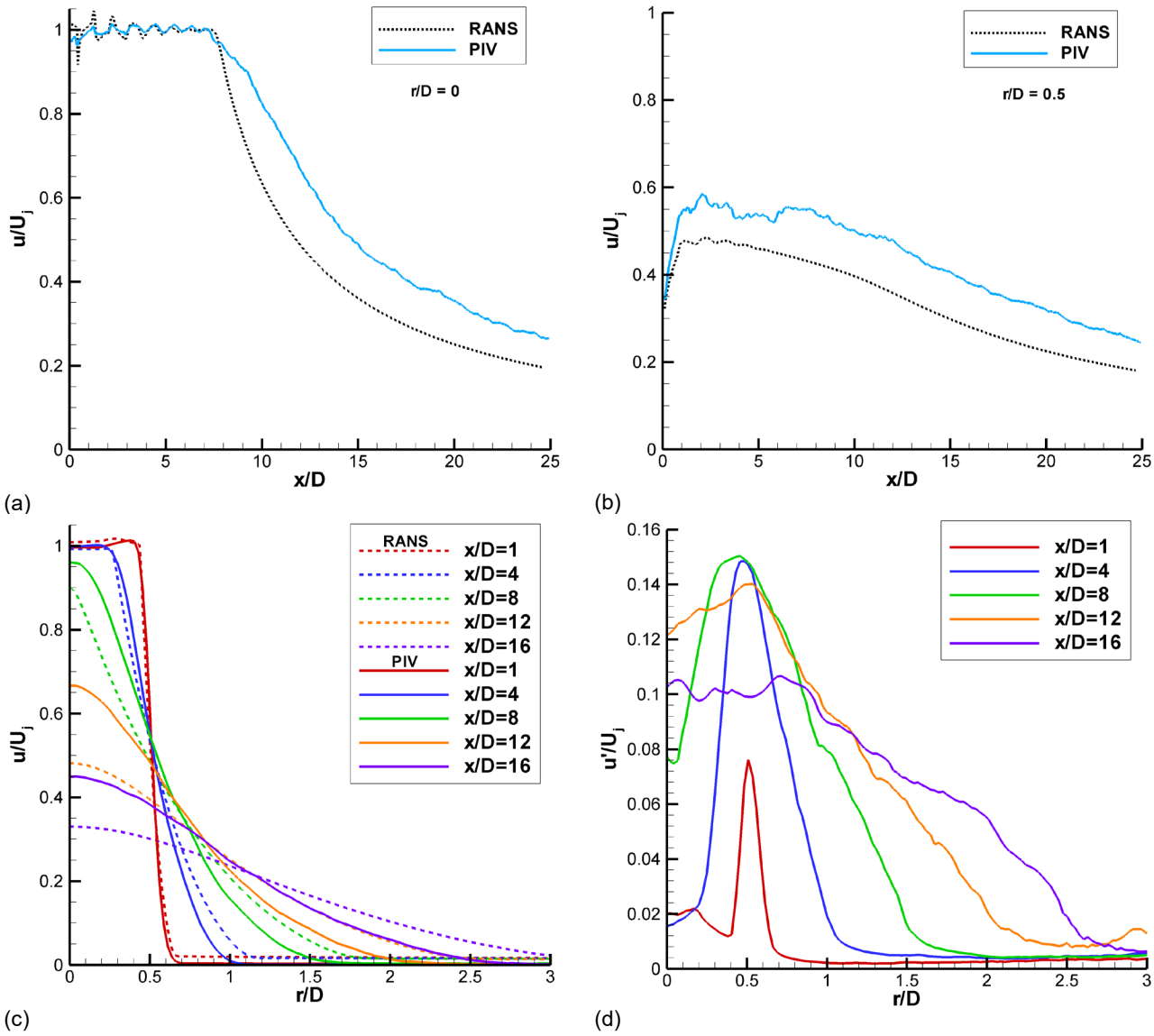

Figure 21.—Comparison of normalized velocity from RANS (dashed lines) and streamwise PIV (solid lines) for SMC015 at Set Point 1402: (a) Centerline (r/D = 0); (b) Lip-line (r/D = 0.5); (c) Radial profiles of normalized mean velocity; (d) Radial profiles of PIV normalized rms velocity, u'/U_j.

number of profiles acquired are shown. The profiles show good agreement between the experiment and the prediction for x/D < 8. The faster decay of the centerline velocity prediction by RANS is the main source of the difference in the radial profile comparison. For completeness, the normalized rms velocities u'/U_j from PIV are plotted in Figure 21(d). The initial low rms velocity fluctuations in the jet core reach their maximum value in the shear layer. The peak rms velocities are low near the nozzle exit due to the spatial averaging of the PIV technique. The higher baseline of the u'/U_j values at x/D = 12 for r/D > 2.5 is due to noise on the PIV camera resulting from the short inter-frame time setting on the camera for this data set.

Figure 22 compares the Raman nondimensional temperature measurements with a RANS solution of the SMC015 nozzle at Set Point 1402. The low-resolution of the Raman centerline profile does not capture the weak shock structures along the jet centerline that are present in the RANS solution. The RANS solution shows an abrupt drop in temperature at the end of the potential core, a known characteristic of the linear 2-equation modeling, rather than the more gradual rounding exhibited by the experimental data. The lip-line nondimensional mean temperature data are shown in Figure 22(b). While

the experimental and RANS velocity profiles along the lip-line were similar, the RANS solution does not exhibit the initial low nondimensional temperature observed in the Raman temperature measurements. This could be due to the adiabatic wall assumption used in the RANS analysis, that results in a modeled trailing edge (or lip) of the nozzle that is indicated to be hotter in the simulation than occurred during the experiment. The radial profile comparison in Figure 22(c) shows generally good agreement between the RANS (dashed lines) and the measured temperatures (solid lines) except for the faster decay of the centerline (r/D = 0) temperatures in the RANS estimates downstream of the potential core (x/D > 8), as already noted in Figure 22(a). In Figure 22(d), radial profiles of the nondimensional rms temperatures are plotted, clearly showing where the region of peak thermal fluctuations broadens and migrates outward with increasing axial distance.

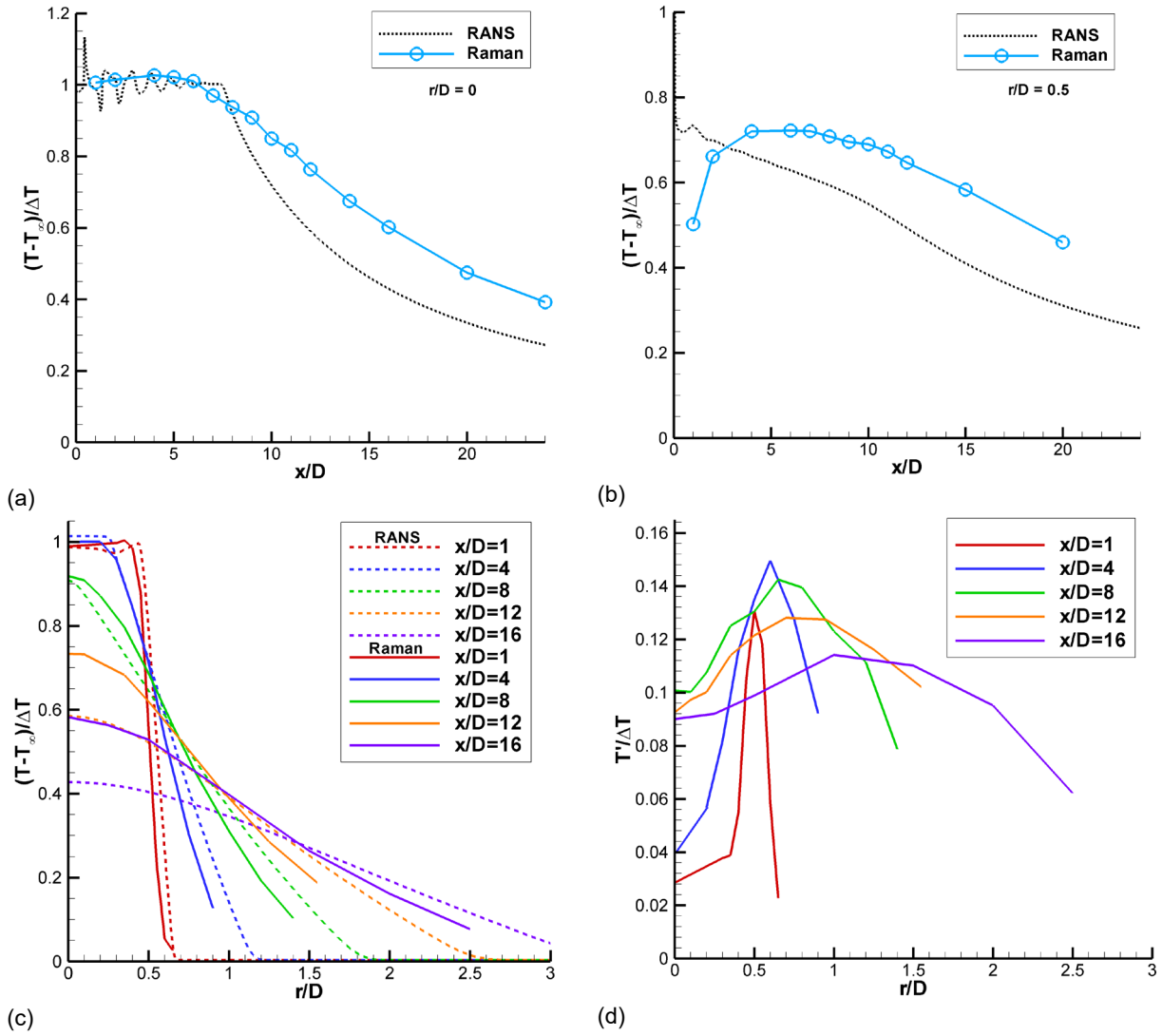

Figure 22.—Comparison of nondimensional temperature from RANS (dashed lines) and Raman (solid lines) for SMC015 at Set Point 1402: (a) Centerline (r/D = 0); b) Lip-line (r/D = 0.5); (c) Radial profiles of nondimensionalized mean temperature from RANS and from Raman; (d) Radial profiles of Raman normalized rms temperature, T′/ΔT.

The processed density estimates from the Raman spectra for SMC015 at Set Point 1402 are plotted in Figure 23. Here the density data are nondimensionalized using the ideally-expanded density at the nozzle exit and the ambient gas density $(\rho_\infty-\rho)/(\rho_\infty-\rho_{Ideal})$. The density data comparison with the RANS solution for both centerline and lip-line in Figure 23(a) and (b), respectively, exhibits the same general trends observed in the temperature comparison. The RANS solution exhibits faster mixing after the potential core and an over prediction of the density on the lip-line near the nozzle exit. The radial profile comparison in Figure 23(c) shows very good agreement within the potential core and then more rapid mixing in the RANS solution relative to the experimental data for the centerline density beyond the end of the potential core, x/D > 8. The nondimensional rms density is plotted in Figure 23(d), where the peak density fluctuations remain relatively constant and both broaden and migrate out radially with increasing axial distance.

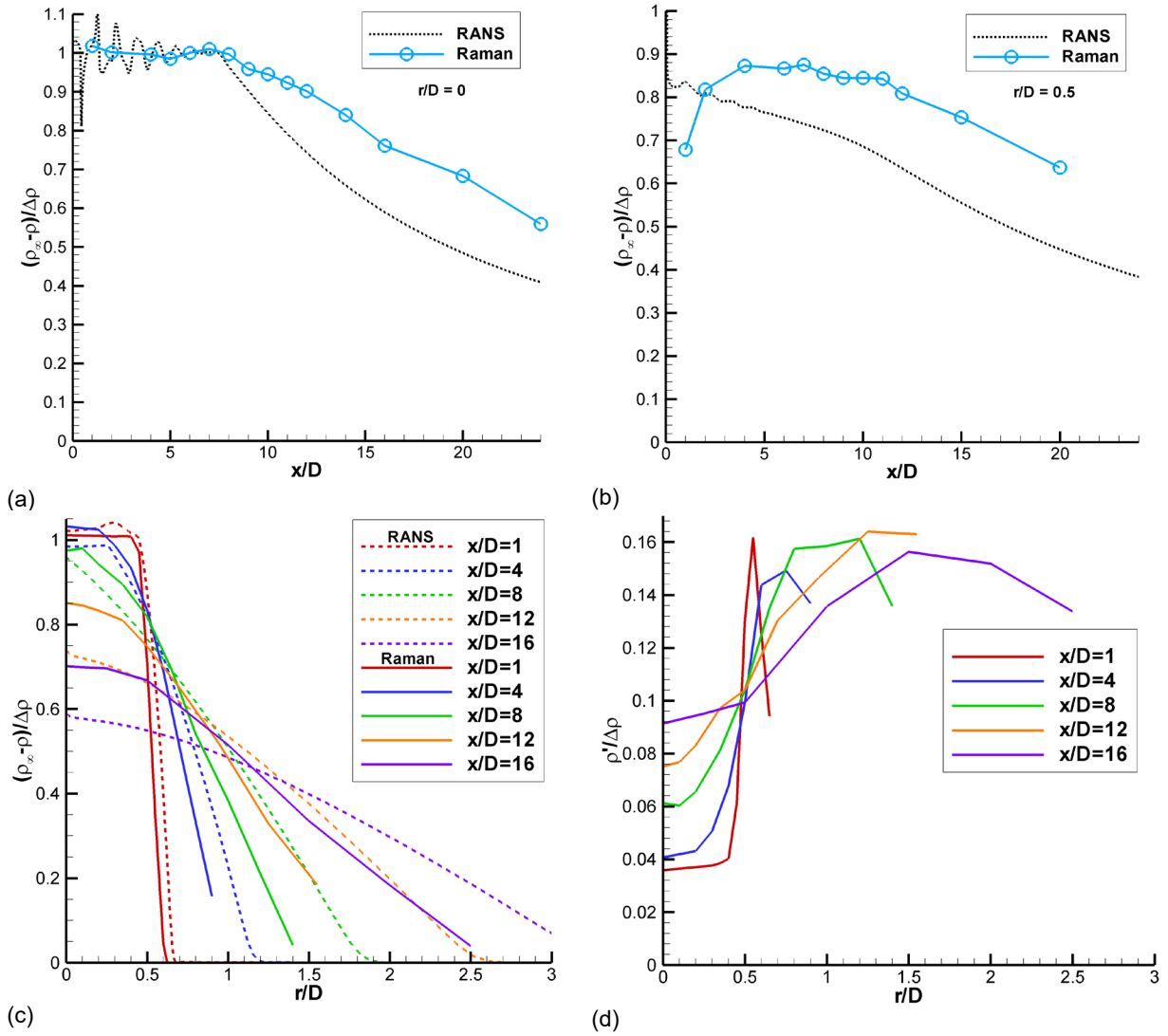

Figure 23.—Comparison of nondimensional density from RANS (dashed lines) and Raman (solid lines) for SMC015 at Set Point 1402: (a) Centerline (r/D = 0); (b) Lip-line (r/D = 0.5); (c) Radial profiles of nondimensionalized mean density from RANS and from Raman; (d) Radial profiles of Raman normalized rms density, $\rho'/\Delta\rho$.

Figure 24(a) shows the radial PIV normalized velocity data (dashed lines) plotted along with the nondimensional Raman temperature (solid lines) data for Set Point 1402. The radial temperature and velocity profiles are similar for $x/D < 4$. Beginning at $x/D = 4$, the nondimensional temperature profiles spread more slowly than velocity. The trend becomes more pronounced with increasing axial distance. Figure 24(b) shows radial profiles of the normalized rms velocity data (dashed lines) plotted along with the normalized rms temperature (solid lines) data. Close to the nozzle exit, the u'/U_j values are likely under-estimated due to the spatial averaging of the PIV correlation subregions. The normalized rms velocities generally peak symmetrically about the lip-line, however; the normalized rms temperatures peak at progressively larger radial locations with increasing axial distance. The peak in $T'/\Delta T$ at larger radial locations with increasing distance downstream is corroborated by the growth in the thermal mixing layer thickness observed in Figure 24(a).

At first glance, the nondimensional radial temperature and density profiles in Figure 22 and Figure 23 appear to be redundant, showing nearly identical trends, however; there is a slight difference in the two profiles. Figure 24(c) shows a radial profile comparison of the Raman nondimensional temperature (solid lines) and density (dashed lines) at increasing axial stations along the jet plume. The nondimensional density profiles exhibit different decay shapes compared to the nondimensional temperature profiles, due to the inverse relationship of density on gas temperature. For $x/D < 2$, the nondimensional temperature and density profiles have similar shape near the jet centerline ($r/D = 0$). However, across the shear layer the two profiles decay at different rates, eventually merging back together outside of the shear layer where the gas temperature has reached the ambient temperature and is no longer changing. Beginning at $x/D = 4$, the profiles of nondimensional temperature start out at a lower normalized magnitude than the corresponding density profiles, although the temperature and density profiles still converge back together at progressively larger r/D values with increasing axial distance. Similar differences in the nondimensional temperature and density profiles were observed in the RANS solution.

The rms temperature and density data in Figure 24(d) are each nondimensionalized by the difference between the value at the jet exit and the ambient value. The magnitude of the two nondimensional rms quantities are nominally the same. However, the nondimensional rms temperatures peak closer to the lip-line of the nozzle, while the nondimensional rms densities peak at progressively larger radial locations with increasing axial distance. Figure 24(e) shows the r/D locations of the peak in the normalized rms u'/U_j, $T'/\Delta T$ and $\rho'/\Delta\rho$ at each axial station. The trajectories of the rms peaks show the velocity fluctuations remain close to the lip line while the peak rms temperature and densities occur at increasingly larger radial locations. The results shown here agree with the previous work of Panda (Ref. 39), where Rayleigh scattering measurements showed that the density shear layer $\rho'/\Delta\rho$ was outboard of the velocity shear layer u'/U_j in heated jets.

The rms data in Figure 24(b) and (d) are normalized by the constant reference values as stated above. The local intensities of the turbulent fluctuations of each of the quantities can be obtained by normalizing the rms values by the local mean values of each of the variables. Figure 25(a) shows radial profiles of the rms temperature intensity (T'/T) and rms density intensity (ρ'/ρ) values, which both peak at the same radial locations. Hence, the expected coupling of the density and temperature fluctuations is confirmed; since the static pressure does not vary significantly across the shear layer. Figure 25(b) shows the radial locations of the peak rms intensities in temperature and density as a function of axial station. The locations of the peak intensity values for both temperature and density are nearly identical.

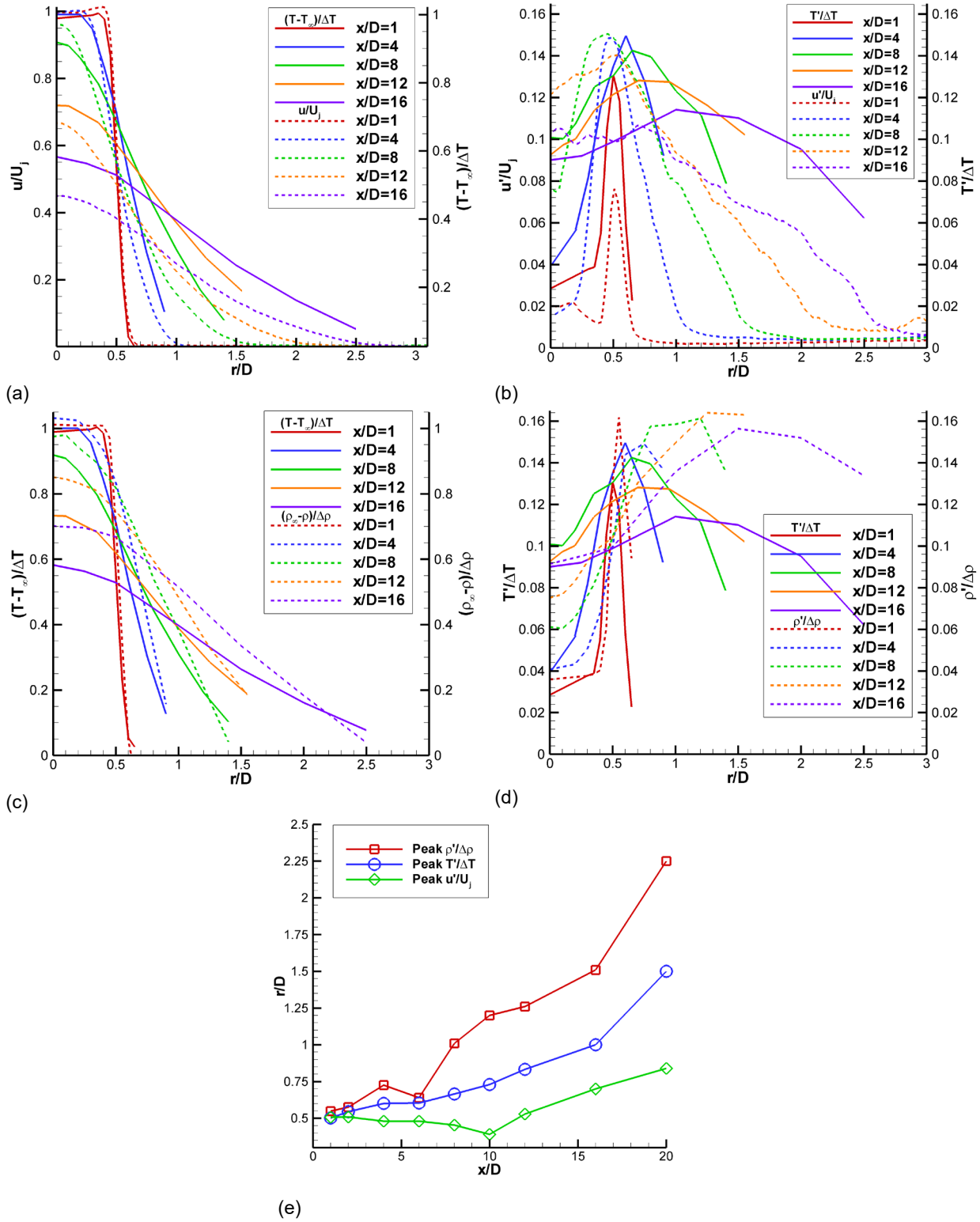

Figure 24.—SMC015 at Set Point 1402: (a) Comparison of radial profiles of PIV u/U_j to Raman $(T-T_\infty)/\Delta T$; (b) comparison of radial profiles of PIV u'/U_j to Raman $T'/\Delta T$; (c) Comparison of radial profiles of Raman $(T-T_\infty)/\Delta T$ to Raman $(\rho_\infty-\rho)/\Delta\rho$; (d) Comparison of radial profiles of Raman $T'/\Delta T$ to Raman $\rho'/\Delta\rho$; (e) Radial locations of the peak rms intensities for u, T and ρ at each axial station.

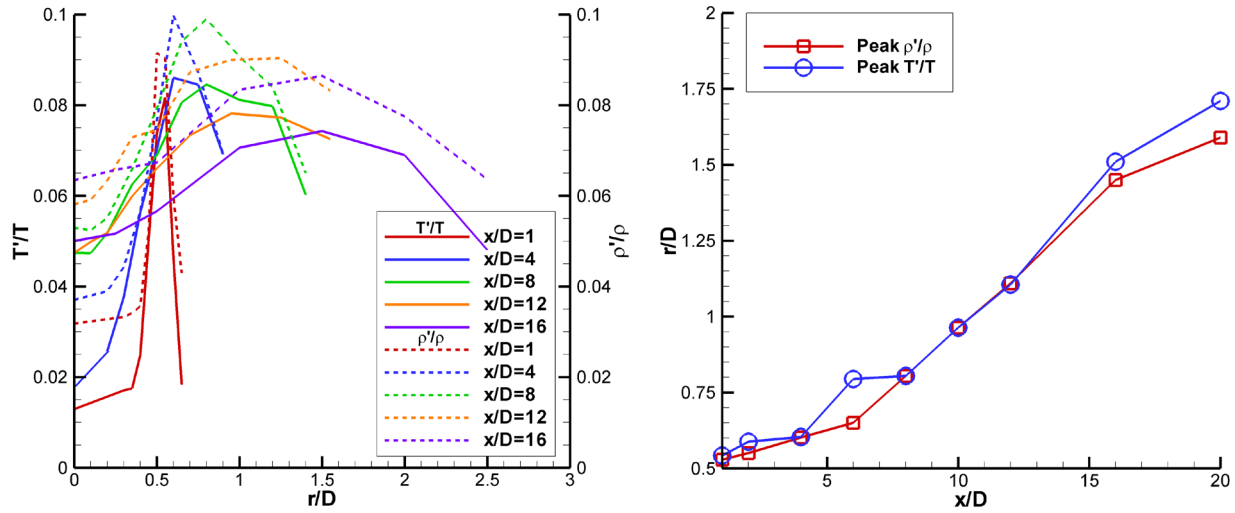

Figure 25.—SMC015 at Set Point 1402: (a) Radial profiles of rms temperature intensity and rms density intensity; (b) Radial locations of the peak rms intensity in temperature and density as a function of axial station.

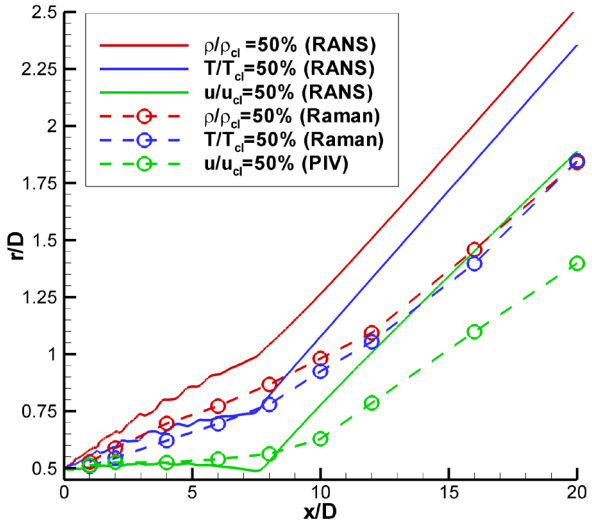

Figure 26.—Locations where the measured RANS, PIV and Raman centerline u, T, and ρ values have dropped to within 50 percent of the ambient value for SMC015 at Set Point 1402.

Figure 26 shows the locations where the RANS predicted and PIV and Raman measured jet properties are exactly halfway between the local centerline and ambient values for the Set Point 1402 case. This is a measure of the global mixing rate for each of the measured quantities. The Raman density and temperature 50 percent peak curves are nearly identical with an initial gradual radial migration outward that increases in slope slightly for x/D > 10. The PIV velocity drops to 50 percent nearly on the lip-line for x/D < 8 and then starts a slow outward radial migration past the end of the potential core. These same general trends are observed in the RANS predictions, computed using $Pr_t = 0.7$, for the Set Point 1402 case. The RANS cases exhibit a more pronounced "knee" region at x/D ≈ 8 due to the sharp end of the potential core previously noted in the RANS solution compared to the more gradual roll-off of the PIV and Raman measurements at the end of the potential core. The faster mixing of the RANS solution results in the higher slope observed in these 50 percent peak curves for x/D > 8 as compared to the shallower slopes observed in the Raman and PIV 50 percent iso-lines.

9.6 SMC015 Set Point 1401 PIV and Raman Results

In many jet studies, the nozzle exit temperature is either significantly above or below the ambient air temperature. For the three different nozzle geometries tested here, a $\Delta T = 0$ set point was used for each nozzle, meaning that the jet core static temperature was matched to the ambient air static temperature. Examination of the PIV radial velocity profiles revealed nothing unusual occurring in the shear layer. However, as stated previously, the BOS data exhibited a localized increase in the gas temperature in the jet shear layer for all of the nozzles at the $\Delta T = 0$ set point. Hence, the resolution and spacing of the Raman temperature radial profile measurement grids for the $\Delta T = 0$ cases were altered to further investigate the feature observed in the BOS data. Conventional approaches for nondimensionalizing the temperature data, such as that used thus far in this report, become problematic when $\Delta T = 0$. Hence, a different approach for presenting the data for the $\Delta T = 0$ case was required. Initially, the Raman temperature data were converted to total temperature T_t by using the streamwise PIV data to provide a local flow velocity measurement at each Raman static temperature measurement location via:

$$T_t = T_s + \frac{u^2}{2C_p} \tag{3}$$

where u is the PIV measured axial velocity and C_p is the specific heat capacity of the gas at constant pressure. In computing T_t, the Raman measured static gas temperature was used to also compute the specific heat of air C_p at 101.325 kPa. The radial profiles of total temperature are more readily nondimensionalized as shown in Figure 27 using total temperature at the jet exit instead of the static temperature, $\Delta T_t = T_{t,j} - T_{t,\infty}$. As plotted here over the full range of temperatures, there is barely any discernable disturbance in the temperature profiles across the nozzle shear layer, unless the region near r/D = 0.5 is magnified. This approach for plotting the $\Delta T = 0$ set point data is not practical for investigating the relatively small-scale thermal flow feature in the shear layer.

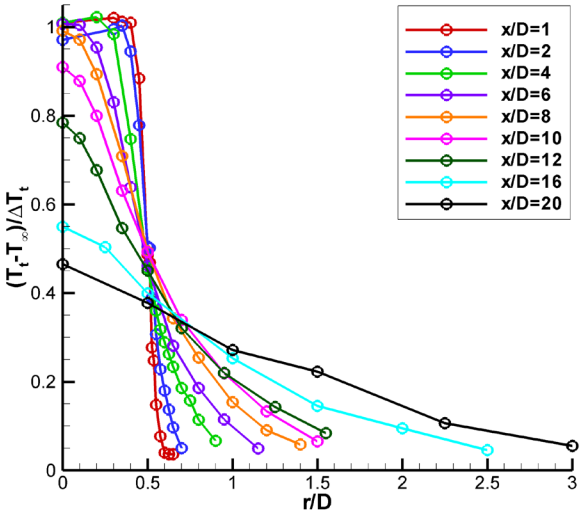

Figure 27.—Nondimensionalized radial total temperature profiles for SMC015 at Set Point 1401.

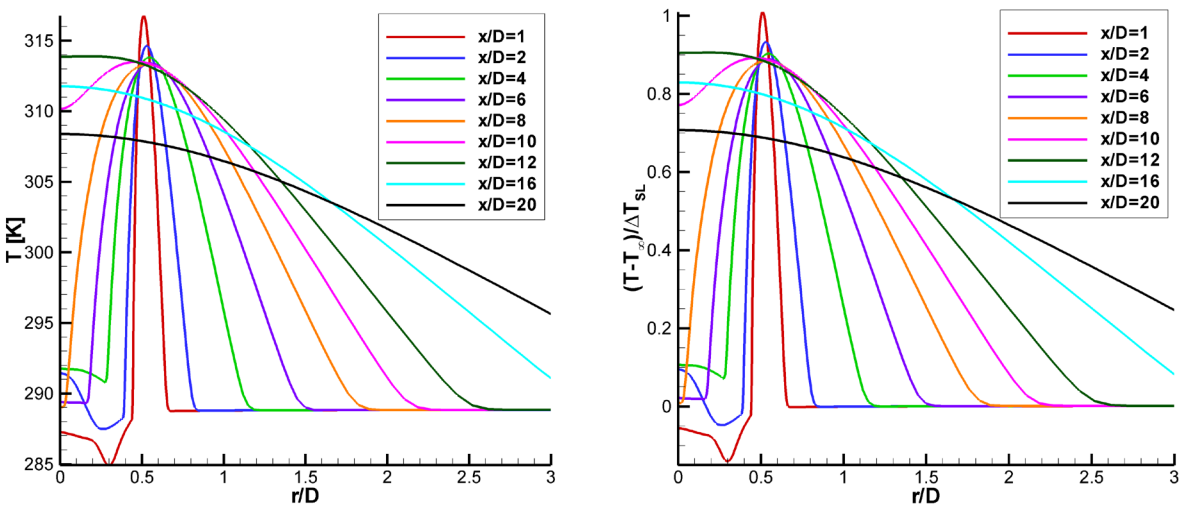

(a) (b)

Figure 28.—RANS solution for SMC015 at Set Point 1401: (a) Raw temperature radial profiles; (b) Nondimensional temperature profiles.

An alternative approach for presenting the $\Delta T = 0$ case data was developed by examining the RANS solution for SMC015 at Set Point 1401. The raw RANS radial temperature profiles are plotted for the $\Delta T = 0$ case in Figure 28(a), where a rise in temperature is observed across the shear layer. Since the standard ΔT (based on the difference between the nozzle exit temperature and the ambient temperature) cannot be used and the nondimensional total temperature masked the temperature feature of interest, the authors propose that the appropriate characteristic temperature difference is the peak temperature across the shear layer at x/D = 1 (T_{SL} = 316.6 K), relative to the ambient temperature (T_∞ = 288.8 K). Applying this shear layer based characteristic temperature difference, ΔT_{SL}, the nondimensional radial RANS profiles are plotted in Figure 28(b), where the desired nondimensional peak temperature of 1 is obtained at the center of the shear layer and the profiles tend to 0 in the ambient. There is some undershoot in the jet core region (x/D < 4), which can be ignored for the purposes of examining the phenomenon of interest across the shear layer.

Applying the same ΔT_{SL} based normalization approach to the Raman temperature profiles enables comparison with the RANS result for the centerline profile as shown in Figure 29(a). For the Set Point 1401 data set, the peak temperature in the shear layer, T_{SL}, was determined to be 301.4 K when T_∞ = 277.1 K. The centerline profile shows an increase in temperature up to approximately x/D = 5 followed by a drop-in temperature before the final rise in temperature at the end of the potential core. Initially, this spike in temperature was believed to be the result of condensation in the nozzle plume. However, after comparison with the RANS solution, it appears that the under-sampling of the nozzle plume via the coarse Raman temperature measurement grid in the potential core yields an aliased depiction of the true sinusoidal temperature profile, due to the weak shocks present in the jet core. The RANS result predicts a slightly shorter potential core length than that measured by Raman. The faster decay of the RANS velocities was also observed when compared to PIV, as shown in Figure 29(b). Note that the PIV data also indicates that the weak shock oscillations persist past the end of the potential core.

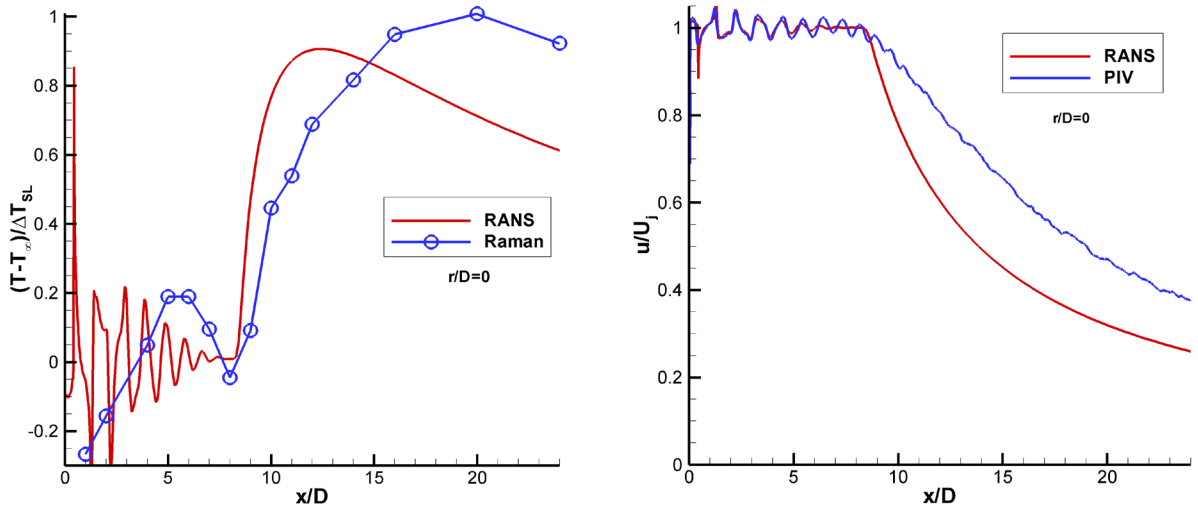

(a) (b)

Figure 29.—Comparison of RANS against Raman for SMC015 at Set Point 1401: (a) Nondimensional centerline temperature profiles; (b) Normalized centerline velocity profiles.

Radial profiles of the mean and rms Raman temperature data normalized by ΔT_{SL} for SMC015 at Set Point 1401 are shown in Figure 30. The radial profiles have a high concentration of points surrounding the expected peak temperature in the shear layer as a function of x/D. The temperature does spike across the shear layer, with the sharpest peaks near the jet exit, as shown in Figure 30(a). The rms profiles in Figure 30(b) show that there is actually a drop in the rms temperature when the temperature peaks in the shear layer. The minima are best observed in Figure 30(c), where an expanded region of the first 4 axial station radial profiles centered about the nozzle lip-line are shown. The drop in rms temperature at the peak temperature in the shear layer suggests that this is the source location of the gas heating, hence the gas is of more uniform temperature at the source, since it has not yet mixed with the cooler gas in the jet core or the ambient. The gas is heating from the turbulent mixing and resultant dissipation along the center of the shear layer, the region of peak shear. The slow diffusion of the heat results in the observed localized temperature increase. Figure 30(d) shows the mean density normalized by the density at the nozzle exit plotted across the shear layer for the first 5 axial stations. The normalized density profiles exhibit a drop in density at the center of the shear layer, which coincides with the peak temperatures measured across the shear layer in Figure 30(a). The Raman measured drop in density is the cause of the drop-in density gradient magnitude observed in the BOS measurements at Set Point 1401.

Finally, the radial profiles of nondimensionalized Raman temperature data are compared against the RANS prediction in Figure 31 for SMC015 at Set point 1401. The RANS profiles are dashed lines and the Raman data are solid lines. The Raman data generally agree with the RANS solution for this case. As shown before for the Set Point 1402 data, the Raman temperature measurements exhibit a slightly faster decay in temperature across the shear layer than the RANS prediction. The limited radial extent of the Raman temperature measurement profiles prevents the data from exhibiting the asymptotic plateau to the ambient temperature, which is observed in the RANS solution.

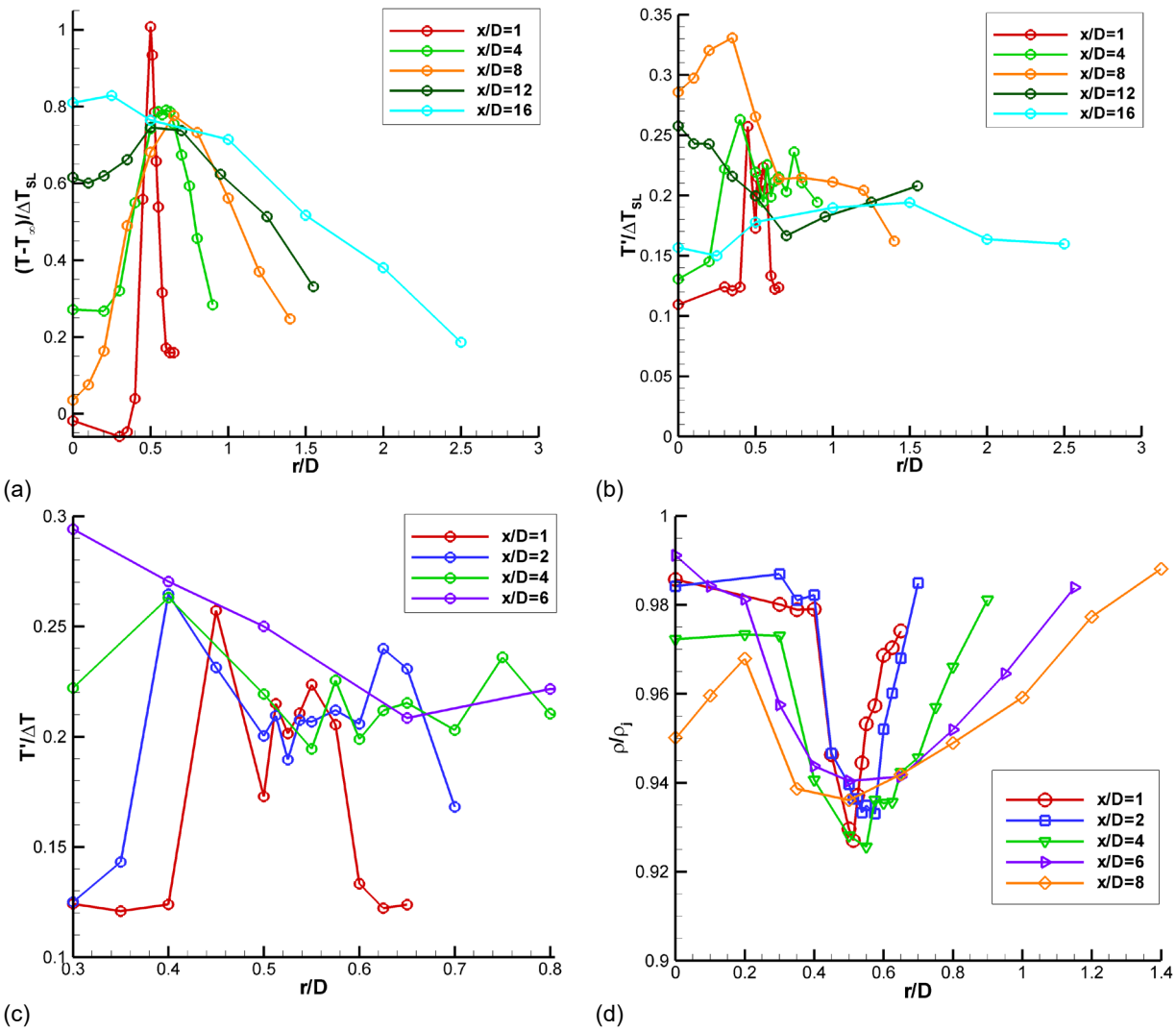

Figure 30.—Nondimensional Raman temperature data for SMC015 at Set Point 1401: (a) Radial profiles of mean temperature; (b) Radial profiles rms temperature; (c) Expanded region of the rms temperature profiles centered about the lip-line; (d) Normalized density measurements across the shear layer.

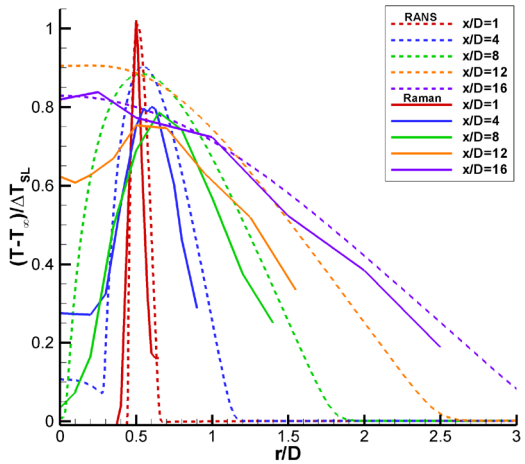

Figure 31.—Comparison of RANS and Raman radial profiles for SMC015 at Set Point 1401.

9.7 SMC017 Set Point 1664 PIV and Raman Results

Almost all of the centerline Raman temperature profiles were acquired at relatively low resolution inside the potential core since measuring the temperatures within the weak shock pattern at the perfectly matched jet exit conditions were not of high importance. For SMC017 at Set Point 1664, the nozzle was run off-design, at an over-expanded condition, with a nozzle pressure ratio corresponding to that of a Mach 1.36 perfectly expanded case. The nozzle supply total pressure would reach equilibrium for a nozzle exit to throat area ratio corresponding to the Mach 1.36 nozzle, hence the effective diameter of the nozzle is given by:

$$D_{eff} = D\sqrt{\frac{\left(A/A^*\right)_{M=1.36}}{\left(A/A^*\right)_{M=1.63}}} \tag{4}$$

which yields D_{eff} = 47 mm.

A high-resolution Raman centerline measurement grid was used to profile the jet centerline at Set Point 1664. The measurement grid used progressively larger spacings, beginning with 6.35 mm increments out to 254 mm, then switching to 12.7 mm increments out to 406.4 mm followed by 25.4 mm increments. The processed, nondimensional temperature and density data are plotted along with the streamwise PIV normalized velocity data in Figure 32(a), where D_{eff} is used to normalize the axial coordinate. Examination of the centerline velocity, temperature and density all indicate that the potential core length is approximately 6 D_{eff}. Because of the significantly over-expanded conditions in the set point 1664 case, not only are there oblique shock waves and expansion waves, but the first compression results in a normal shock near the nozzle exit and at the centerline. From the RANS solution, this normal shock, (also referred to as a Mach disk) results in a loss of total pressure such that the downstream total pressure is 0.881 times the plenum total pressure. Further, while the perfectly expanded Mach number for the set point 1664 conditions is 1.36, with the drop in total pressure caused by the normal shock, the new equilibrium Mach number is 1.267. The equilibrium values of jet properties, namely velocity, temperature, and density, are 0.948, 1.036, and 0.965 times the perfectly expanded jet potential core values, respectively. In other words, these are the mean values that the post-normal shock centerline jet quantities oscillate upon through the rest of the potential core. Note that the reference values used in the nondimensionalizations for both experimental and computational results in Figure 32 employ the perfectly expanded jet quantities. The sinusoidal oscillations of the nondimensional velocity and temperature within the potential core are exactly out of phase, as expected. The nondimensional density peaks are also out of phase with the nondimensional temperature peaks due to their inverse temperature dependence. The magnitude of the nondimensional density peaks are the largest, followed by the oscillations in the nondimensional temperature profile. The nondimensional velocity peaks are the lowest, possibly due to the spatial averaging of the PIV data. The temperature and density decay a little more slowly than the velocity downstream of the potential core, as also observed in the Set Point 1402 case in Figure 22(c). For comparison, a RANS solution for Set Point 1664 is shown in Figure 32(b). The RANS solution shows slightly higher oscillations in temperature and density and also slightly over-predicts the length of the potential core, out to 8 D_{eff}. The decay of the flow properties downstream of the potential core agrees very well between experiment and the RANS prediction. Both the flow measurements of velocity, temperature and density and the RANS prediction denote the existence of the double shock peak in the 2nd shock cell as previously reported by Raman (Ref. 40). The double shock peak is most readily visible as a “shoulder” on the 2nd temperature peak ($x/D_{eff} \approx 1.5$), but is also evident in the minima in the velocity profiles at $x/D_{eff} \approx 1.5$.

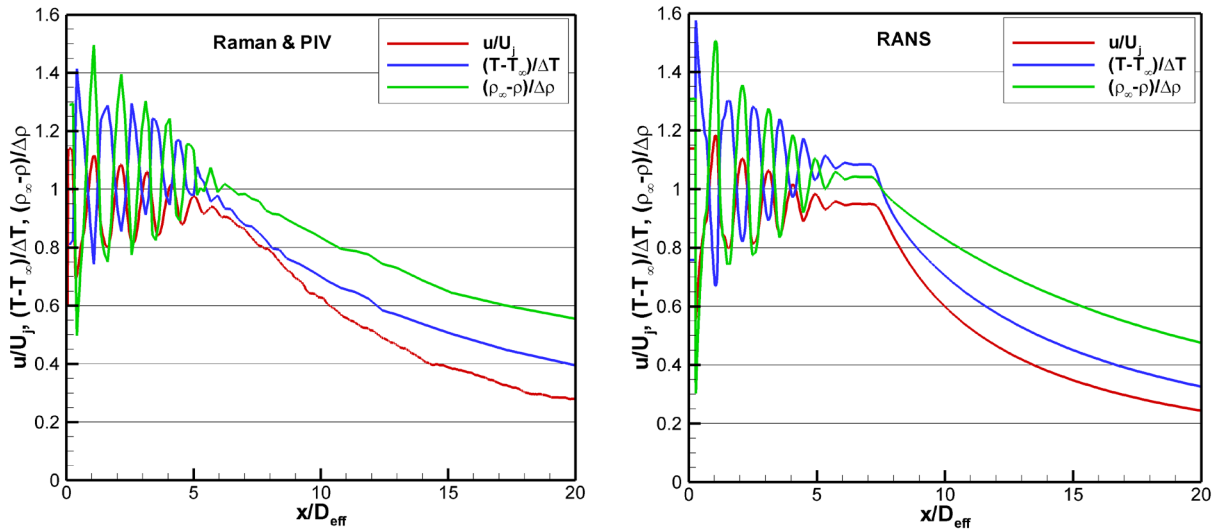

Figure 32.—Comparison of nondimensional mean velocity temperature, and density for the over-expanded jet condition on SMC017 at Set Point 1664 for (a) Raman and PIV; (b) RANS.

9.8 Shock Cells Beyond the Potential Core

In the discussion of the centerline velocity profile in Figure 29(b), it was noted that the velocity oscillations due to the shock cells within the jet potential core, actually persisted past the end of the potential core. This phenomenon was also observed in Figure 20(a) and Figure 31(a) and has been reported in other supersonic jet flow studies (Refs. 41 to 43). At the end of the time-averaged potential core, the shear layers have merged and the high turbulence in this region should dominate the flow. However, examination of the individual velocity vector maps reveals that the length of the potential core changes, due to instabilities in the jet plume. The streamwise PIV instantaneous velocity vector maps collected for Set Point 1664 were examined in more detail to investigate the persistence of the oscillations past the end of the potential core. The dual side-by-side streamwise PIV cameras provided a 355 mm wide field of view, covering 7.5 D_{eff}. The processed velocity vector maps were processed to find and count the number of shock cells in the jet plume. A contour map of one instantaneous velocity vector map is shown in Figure 33(a). A threshold level of 597 m/s was used to isolate the peak velocity regions of the shock cells, yielding the "binarized" image shown in Figure 33(b). The individual shock cells were processed using a "blob" analysis algorithm to detect their location and size. A minimum shock cell size of at least 30 percent of the primary shock cell was imposed to limit the number of detected shock cells. Figure 33(c) shows the results of the identified and labelled shock cells, where nominally 4 shock cells were identified for the velocity field in Figure 33(a). Note that the normal shock at the exit of the nozzle, labeled as 0, is not included in the total shock cell count. Another instantaneous velocity vector map is shown in Figure 34(a), which has a longer string of shock cells. Thresholding the velocity map reveals 9 potential shock cells as shown in Figure 34(b). The processed and labelled "blobs" are shown in Figure 34(c), where 7 shock cells have passed the selection criteria. The average velocity vector map for Set Point 1664 at the first axial station is shown in the contour plot in Figure 35(a). The sequence of 400 vector maps were processed using the blob analysis and the results compiled into a histogram shown in Figure 35(b) where the number of occurrences is plotted against the number of shock cells in the jet plume. The histogram reveals that nearly half of the time the jet plume has 5 shock cells, and 13 percent of the time it has 4 shock cells. Nearly 30 percent of the time there are 6 shock cells and approximately 7 percent of the time there are 7 or more shock cells. The analysis proves that the length of the shock cell

train is changing in time. The size and location of the first 4 shock cells is relatively constant. Beyond 4 D_{eff}, the shock cell train is less stable as large-scale turbulent structures distort the jet plume/shock cells breaking them into smaller cells. These large structures "stretch" the shock cell train leading to the higher cell count shock trains, where the shock cells persist further downstream than the time-averaged potential core length of the plume. After the passage of a large structure, the shock cell train "snaps" back, yielding the shortened shock cell train (4 cells). Averaging the ensemble of measurements yields a mean centerline flow field with weak oscillations that persist past the end of the potential core, which is in agreement with the observed oscillations in Figure 21(a), Figure 29(b), and Figure 32(a).

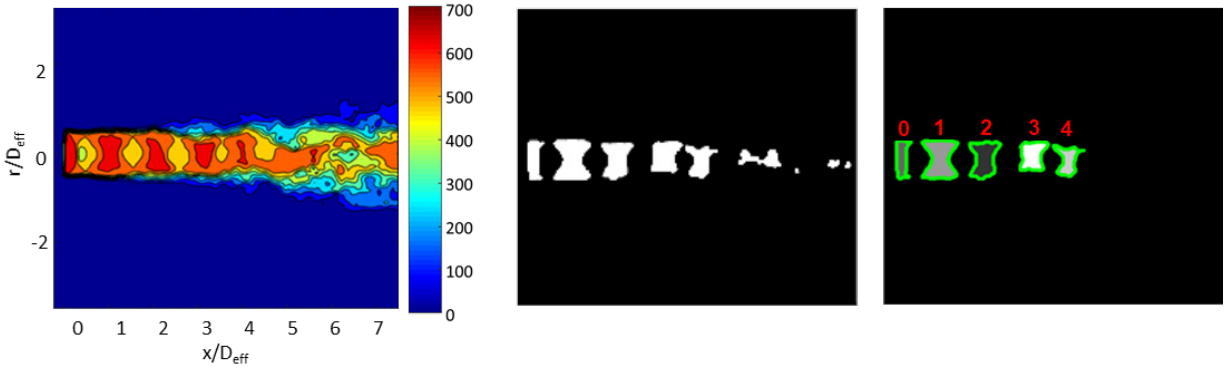

(a) (b) (c)

Figure 33.—Set Point 1664: (a) Instantaneous velocity map; (b) Threshold limited velocity map showing isolated shock cells; (c) Processed blob map showing the jet plume only contains 4 shock cells after the normal shock at the jet exit.

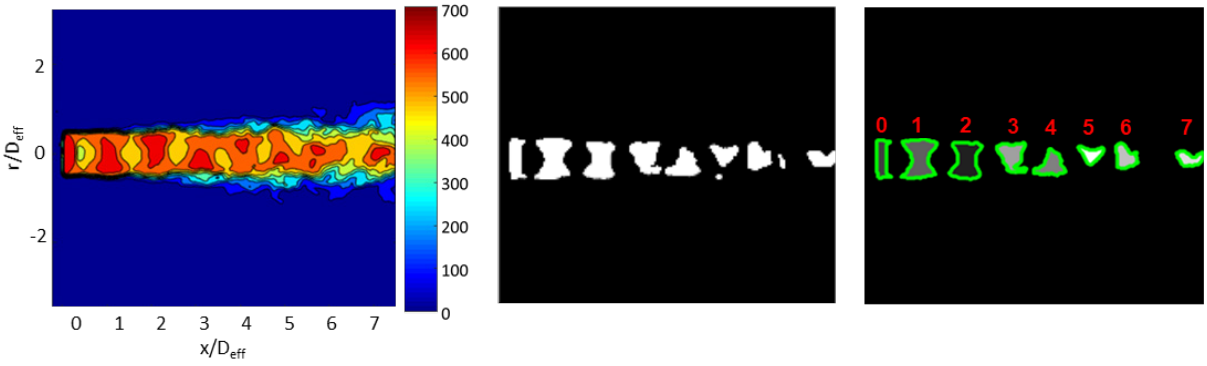

(a) (b) (c)

Figure 34.—Set Point 1664: (a) Another instantaneous velocity map; (b) Thresholding the velocity map defines the isolated shock cells; (c) Processed blob map showing the jet plume contains 7 shock cells after the normal shock at the jet exit.

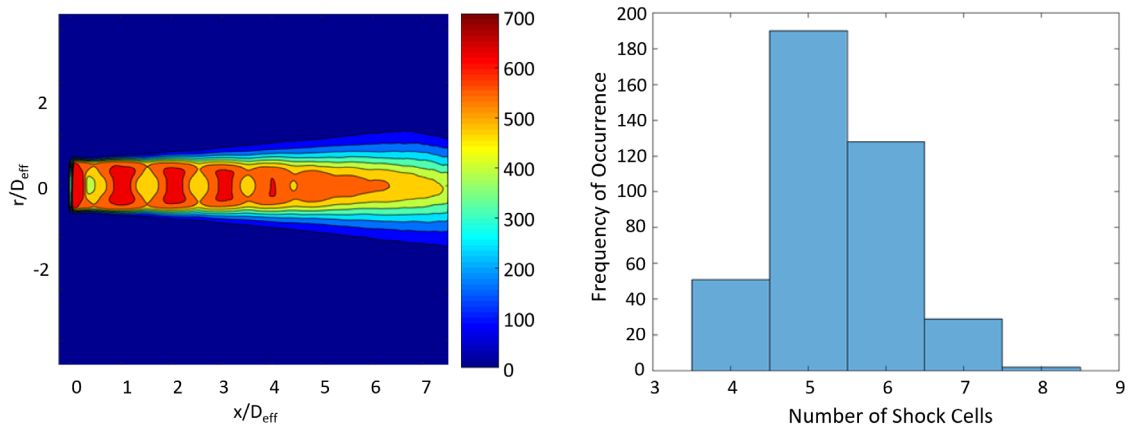

Figure 35.—(a) Mean velocity for the first axial station at Set Point 1664; (b) Histogram of the number of occurrences of the shock cells in the jet plume.

9.9 SMC020 PIV and Raman Results

One of the main objectives of this test program was to compare the data sets collected here using nonintrusive measurements with the widely used legacy data of Seiner et al. (Ref. 1). This data set has been widely used for three decades to validate supersonic jet and compressible mixing CFD prediction methods, hence validating the data set with modern tools is of high importance. The SMC020 nozzle installed on the SHJAR was only capable of matching three of the test conditions measured by Seiner: Set Points 2001, 2002 and 2004 corresponding to Seiner's surveys at $T_{t,Plenum}$ = 313 K (563 R), 508 K (915 R), and 755 K (1359 R). Both the streamwise and cross-stream PIV data are compared against the Seiner data sets in Figure 36. The streamwise data are drawn as lines and the cross-stream data are represented by symbols extracted at the center of the jet plume, at r/D = 0. The data are nondimensionalized as described previously. At the lowest total temperature, 313 K, there was significant condensation in the shear layer and at the end of the potential core. The condensation makes imaging individual PIV seeding particles in the flow problematic, hence there is a loss of correlation in these regions. The PIV data are only valid out to approximately 15 D for Set Point 2004. In all three cases illustrated in Figure 36, the PIV data matches extremely well with the historical probe data. The PIV data again indicate that the shock cell oscillations persist well past the end of the potential core, as observed previously in Figure 29(b).

Next, the Raman temperature data are compared to the Seiner data set. Condensation in the flow prevented any temperature data from being collected at the lowest total temperature case of 313 K. At the two elevated temperatures, there was still some condensation in the jet shear layer and downstream of the potential core but not enough to preclude successful temperature measurements. For the data comparison, the streamwise PIV data was again used to convert the Raman static temperature measurements into total temperature T_t. The total temperatures are plotted in Figure 37(a), where the Seiner probe data are plotted with solid lines and the Raman data are plotted with dashed lines/symbols. The Set Point 2001 case has a total temperature at the nozzle exit of approximately 523 K (942 R). The Raman total temperature results closely parallel the Seiner probe measurements at $T_{t,Plenum}$ = 508.2 K within the potential core but show a faster decay than the Seiner data after the potential core. For the Set Point 2002 case, $T_{t,Plenum}$ is approximately 742 K, which is slightly lower than the probe measurements at $T_{t,Plenum}$ = 755.4 K. The Raman data lie just below the probe measurements but track the shape of the Seiner data almost exactly. Again, the historical probe data are of good quality and agree with the modern nonintrusive flow

diagnostics. For completeness, the Seiner data at 1116 K and the Set Point 2003 data set at 924 K are also included in Figure 37(a). The total temperature profiles exhibit the same general trends. Figure 37(b) shows the same T_t profiles normalized by $T_{t,Plenum}$. The direct comparisons of the Seiner results to the THX5 data are very good at $T_{t,Plenum}$ = 508 K and 755 K. The higher temperature THX5 and Seiner profiles at $T_{t,Plenum}$ = 924 K and 1116 K respectively, illustrate the continued temperature dependence of the centerline normalized total temperature profiles.

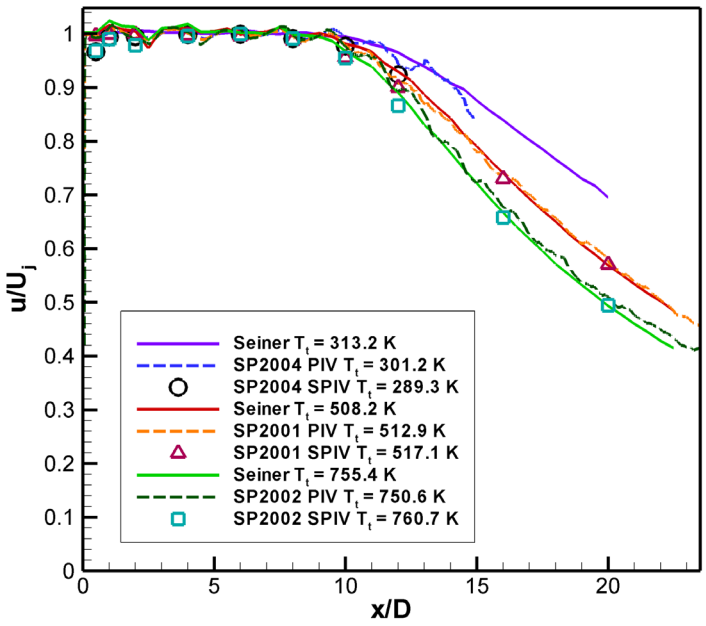

Figure 36.—Comparison of the Seiner probe data to both streamwise and cross-stream PIV data.

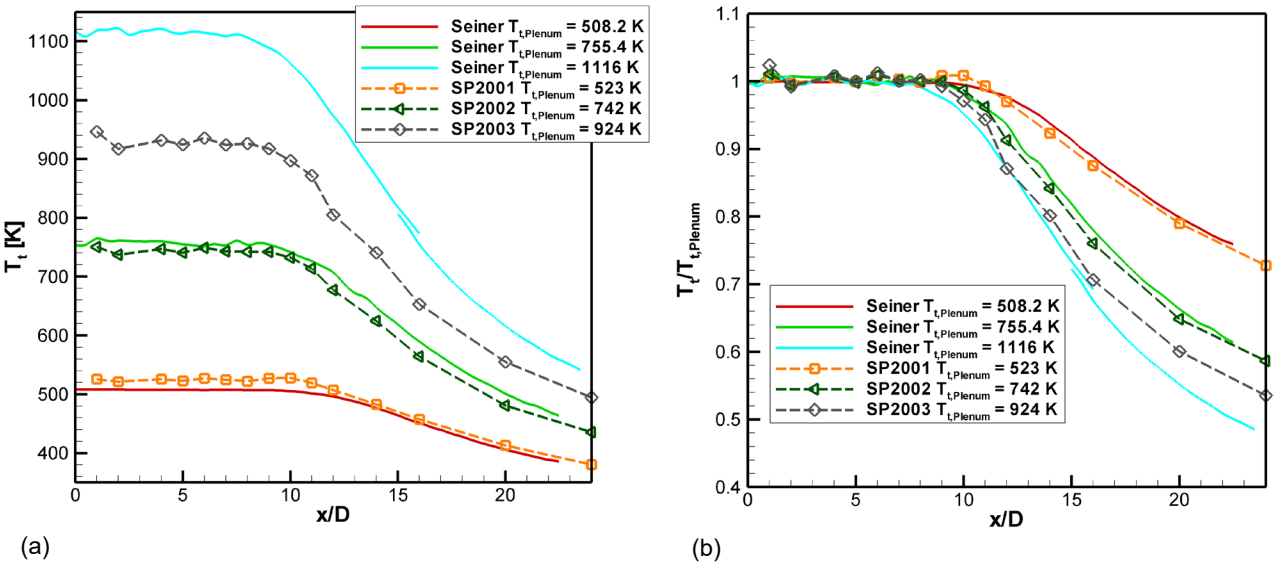

(a) (b)

Figure 37.—(a) Comparison of Raman total temperature measurements with historical probe data for SMC020 at Set Points 2001 and 2002. Results from higher temperature surveys from both THX5 and Seiner et al. (Ref. 1) are also included; (b) Normalized T_t profiles illustrating the effect of temperature on the total temperature surveys.

10.0 Conclusions

A series of supersonic nozzles were tested across a range of temperatures in order to replicate and expand the Mach 2.0 probe measurements of Seiner et al. (Ref. 1). Three different 50.8 mm exit diameter nozzle designs were tested with perfectly expanded Mach numbers of 1.36, 1.63, and 2.0. The temperature difference between the jet core and the ambient was held at fixed values of 0 K, 133 K, 233 K; and then also run at –128 K for the Mach 2.0 nozzle and 333 K for the Mach 1.36 nozzle. Probe surveys of the nozzles essentially repeated the measurements of Seiner, et al., (Ref. 1). The probe measurements generally showed good agreement with the historical measurements but exhibited a slightly faster decay in velocity and temperature after the potential core, possibly due to heat transfer related to the large rake and supporting hardware of the THX5 probes. An improved algorithm for extracting Mach number from the total pressure measurements was also presented. Next, modern optical diagnostics were used to study the flow. The modern techniques significantly expanded the spatial extent and properties of the flow field that were measured, adding off-centerline characterization of the flow on the nozzle lip-line and across the shear layer and measurements of static temperature and density.

The RT-BOS system enabled optimization of the SHJAR operating pressure and temperature settings to yield a nearly shock-free, perfectly-matched flow condition. The RT-BOS data quickly revealed an unanticipated feature in the $\Delta T = 0$ case, a low-density region running down the center of the shear layer. This low-density region is coincident with the Raman measured high-temperature region, which is due to the local mixing and heating of the gas at a faster rate than the thermal energy can diffuse. The small magnitude of the flow feature is not normally observed in flows where the nozzle exit temperature is significantly higher or lower than the ambient air. The BOS data facilitated the optimization of the Raman radial measurement profiles to capture the same phenomena in the shear layer profiles.

Streamwise centerline PIV measurements along with cross-stream PIV measurements were acquired. Some of the lower temperature Set Points resulted in significant condensation in the shear layer and at the end of the potential core, limiting the efficacy of the PIV measurements only for the lowest $\Delta T = –128$ K case. Generally, the PIV data showed the relative decrease of the potential core length with increasing jet exit temperature and increasing Mach number.

Rotationally resolved Raman spectroscopy provided unobtrusive measurements of both mean and rms temperature measurements of the jet plume. In addition, the Raman spectra were further processed to extract mean and rms density measurements across the jet plume. Lab scale measurements were used to validate and develop the Raman based density measurement capability used here. In order to compare the modern nonintrusive techniques with the historical probe data, the streamwise PIV velocity data were combined with the Raman static gas temperature measurements to yield total temperature measurements of the nozzle flows. The Raman temperature data showed good agreement with the historical probe data, adding credibility to this widely used database of measurements. Furthermore, the Raman temperature and density data along with PIV measurements were compared against RANS solutions of the nozzle flows, generally showing good agreement at the lower Mach number nozzles and increasing under prediction of the potential core length with the higher Mach number nozzles.

The Raman data confirmed the BOS measurements of the temperature spike along the centerline of the shear layer for the $\Delta T = 0$ cases. The RANS solution also illustrated this feature across the shear layer. At first glance, the density and temperature measurements extracted from the Raman spectra may appear to be redundant, however; as shown here, comparison of the density and temperature mean profiles across the shear layer showed that the profiles decayed at different rates, due to the inverse temperature dependence of the gas density. The rms temperature intensity and rms density intensity were demonstrated to peak at the same radial locations across the shear layer, illustrating the consistency of the

two different flow field property measurements extracted from the Raman spectra. The nondimensional velocity and temperature profiles did not decay at the same rate across the shear layer.

For several of the perfectly matched jet exit conditions and for the over-expanded jet condition, oscillations along the jet centerline were observed past the end of the potential core. Application of a velocity threshold to each instantaneous PIV velocity map facilitated identifying and counting the number of shock cells, which revealed that the length of the shock cell train changes over time due to the interaction/distortion of the shock cell train by large-scale turbulent structures. These interactions lead to lengthening and shortening of the number of shock cells, which when time averaged, yields oscillations in the centerline jet velocity past the end of the traditionally assumed potential core.

The comprehensive measurements of velocity, temperature and density provide a valuable database for use in validating and assessing the prediction capabilities of computational fluid dynamics codes in the challenging environment of supersonic compressible nozzle flows. These data are available as mentioned in the statement below the Abstract from the NASA STI office.

References

1. Seiner, J.M., Ponton, M.K., Jansen, B.J., Lagen, N.T., "The effects of temperature on supersonic jet noise emission," Paper DGLR/AIAA 92-02-046, DGLR/AIAA 14th Aeroacoustics Conference, Aachen, Germany, May 11–14, 1992.
2. Laurence J., "Intensity, scale and spectra of turbulence in mixing regions of free subsonic jets," NASA Report 1292, 1956.
3. Bradshaw, P., Ferris, D.H., and Johnson, R.F., "Turbulence in the noise producing region of a circular jet," *J. Fluid Mech*., Vol. 19, 1964, pp. 591–624. https://doi.org/10.1017/S0022112064000945
4. Albertson, C.W. and Bauserman, W.A., "Total temperature probes for high-temperature hypersonic boundary-layer measurements," NASA-TM-4407, 1993.
5. Ames Research Staff, "Equations, tables, and charts for compressible flow," NACA Report 1135, 1953.
6. Lau, J.C., Morris, P.J., and Fisher, M.J., "Measurements in subsonic and supersonic free jets using a laser velocimeter," *J. Fluid Mech*., Vol. 93, 1979, pp. 1–27. https://doi.org/10.1017/S0022112079001750
7. Lau, J.C., "Effects of exit Mach number and temperature on mean-flow and turbulence characteristics in round jets," *J. Fluid Mech*., Vol. 105, 1981, pp. 193–218. https://doi.org/10.1017/S0022112081003170
8. Bridges, J. and Wernet, M.P., "Measurements of the aeroacoustic sound source in hot jets," AIAA–2003–3130, May, 2003. https://doi.org/10.2514/6.2003-3130
9. Locke, R.J., Wernet, M.P., Anderson, R.C., "Rotational Raman-based temperature measurements in a high-velocity turbulent jet," *Meas. Sci. Technol*., Vol. 29, No. 1, 2017. https://doi.org/10.1088/1361-6501/aa934d, also published as NASA/TM—2017-219504.
10. Bridges, J. and Wernet, M.P., "The NASA subsonic jet particle image velocimetry (PIV) dataset," NASA/TM—2011-216807, 2011. https://ntrs.nasa.gov/citations/20110023688
11. Panda, J. and Seasholtz, R.G., "Velocity and temperature measurement in supersonic free jets using spectrally resolved Rayleigh scattering," AIAA–99–0296, January, 1999. https://doi.org/10.2514/6.1999-296
12. Panda, J. and Seasholtz, R.G., "Investigation of density fluctuations in supersonic free jets and correlation with generated noise," AIAA–2000–2099, June, 2000. https://doi.org/10.2514/6.2000-2099

13. Panda, J., Seasholtz, R.G., Elam, K.A., "Investigation of noise sources in high-speed jets via correlation measurements," *J. Fluid Mech.*, Vol. 537, 2005, pp. 349–385. https://doi.org/10.1017/S0022112005005148
14. Mielke, A. F., Elam, K. A., "Dynamic measurement of temperature, velocity, and density in hot jets using Rayleigh scattering," *Exp. in Fluids*, Vol. 47, No. 6, 2009, pp. 673–688. https://doi.org/10.1007/s00348-009-0708-4
15. Cutler, A.D., Magnotti, G., Cantu, L., Gallu, E., Rockwell, R. and Goyne, C., "Dual-pump coherent anti-stokes Raman spectroscopy measurements in a dual-mode scramjet," *J. Propulsion and Power*, Vol. 30, No. 3, 2014, pp. 539–549. https://doi.org/10.2514/1.B34964
16. Tedder, S., Danehy, P., Magnotti, G., Cutler, A., "CARS temperature measurements in a combustion-heated supersonic jet," AIAA–2009–0524, January, 2009. https://doi.org/10.2514/6.2005-616
17. Kuehner, J.P., Tessier, A.F., Kisoma, A., Flittner, J.G., McErlean, M.R., "Measurements of mean and fluctuating temperature in an underexpanded jet using electrostrictive laser-induced gratings," *Exp. in Fluids,* Vol. 48, 2010, pp. 421–430. https://doi.org/10.1007/s00348-009-0746-y
18. Ajrouche, H., Vervisch, P., Lo, A., Cessou, A., "1D single-shot thermometry in flames by spontaneous Raman scattering through a fast electro-optical shutter," 17th International Symposium on Applications of Laser Techniques to Fluid Mechanics Lisbon, Portugal, 2014.
19. Maté, B., Tejeda, G., Montero, S., "Raman spectroscopy of supersonic jets of CO_2: density, condensation, and translational, rotational, and vibrational temperatures," *J. Chem. Phys.*, Vol. 108, 1998, pp. 2676–2685. https://doi.org/10.1063/1.475660
20. Wernet, M.P., Georgiadis, N.J., Locke, R.J., "PIV and rotational Raman-based temperature measurements for CFD validation in a single injector cooling flow," NASA/TM—2018-219739, 2018. https://ntrs.nasa.gov/archive/nasa/casi.ntrs.nasa.gov/20180000917.pdf
21. Wernet, M.P., Georgiadis, N.J., Locke, R.J., Thurman, D., Poinsatte, P., "PIV and rotational Raman-based temperature measurements for CFD validation of a perforated plate cooling flow Part 1," NASA/TM—2019-220227, 2019. https://ntrs.nasa.gov/archive/nasa/casi.ntrs.nasa.gov/20190029113.pdf
22. Yoder, D.A., DeBonis, J.R., and Georgiadis, N.J., "Modeling of turbulent free shear layer flows," Computers & Fluids, Vol. 117, 2015, pp. 212–232. https://doi.org/10.1016/j.compfluid.2015.05.009
23. Reynolds, A.J., *Turbulent Flows in Engineering*, John Wiley and Sons, New York, 1974.
24. Yoder, D.A., "Comparison of turbulent thermal diffusivity and scalar variance models," AIAA–2016–1561, January, 2016. https://doi.org/10.2514/6.2016-1561
25. Bridges, J. and Wernet, M.P., "Turbulence associated with broadband shock noise in hot jets," AIAA–2008–2834, May, 2008. https://doi.org/10.2514/6.2008-2834
26. Ferraro, J.R., and Nakamoto, K., *Introduction to Raman Spectroscopy*, Academic Press, San Diego, CA, 1994.
27. Wernet, M.P., "Software for acquiring image data for PIV," NASA Tech Briefs November, 2003, pp. 7. https://ntrs.nasa.gov/archive/nasa/casi.ntrs.nasa.gov/20110023930.pdf
28. Wernet, M.P., "Symmetric phase only filtering: a new paradigm for DPIV data processing," *Meas. Sci. Technol.,* Vol. 16, No. 3, 2005, pp. 601–618. https://doi.org/10.1088/0957-0233/16/3/001
29. Taylor, J.R., *An introduction to error analysis*, University Science Books, Oxford University Press, Mill Valley, 1982, pp. 142–144.
30. Wernet, M.P. and Hadley, J.A., "A high temperature seeding technique for particle image velocimetry," *Meas. Sci. Technol.*, Vol. 27, No. 12, 2016. https://doi.org/10.1088/0957-0233/27/12/125201

31. Melling A., "Tracer particles and seeding for particle image velocimetry," *Meas. Sci. Technol.*, Vol. 8, No. 12, 1997, pp. 1406–1416. https://doi.org/10.1088/0957-0233/8/12/005
32. Wernet, M.P., "Real-time background oriented Schlieren: catching up with knife edge Schlieren," NASA/TM—2019-220144, 2019. https://ntrs.nasa.gov/citations/20190002831
33. Wernet, M.P., "Real-time background oriented Schlieren with self-illuminated background," *Meas. Sci. Technol.,* Vol. 31, No. 1, 2019. https://doi.org/10.1088/1361-6501/ab4211
34. Yoder, D.A., Wind-US User's Guide – Version 4.0, NASA/TM—2016-219145, 2016.
35. Menter, F.R., "Improved Two Equation k-ε Turbulence Models for Aerodynamic Flows," NASA-TM 103975, 1992.
36. Menter, F.R., "Two equation eddy-viscosity turbulence models for engineering applications," *AIAA Journal*, Vol. 32, No. 8, 1994, pp. 1598–1605. https://doi.org/10.2514/3.12149
37. Pointwise® [software package], Ver. 17.1 Release 4, Pointwise, Inc., Fort Worth, TX, 2013.
38. Georgiadis, N.J., Yoder, D.A., and Engblom, W.A., "Evaluation of modified two-equation turbulence models for jet flow predictions," *AIAA Journal*, Vol. 44, No. 12, 2006, pp. 3107–3114. https://doi.org/10.2514/1.22650
39. Panda, J., Seasholtz, R., Elam, K., Mielke, A. and Eck, D., "Effect of heating on turbulent density fluctuations and noise generation from high speed jets," AIAA–2004–3016, May, 2004. https://doi.org/10.2514/6.2004-3016
40. Raman, G., "Advances in understanding supersonic jet screech: review and perspective," *Progress in Aerospace Sciences,* Vol. 34, No. 1, 1998, pp. 45–106. https://doi.org/10.1016/S0376-0421(98)00002-5
41. Wishart, D.P. and Krothepalli, A., "On the structure of a heated supersonic jet," AIAA-94-0666, January, 1994. https://doi.org/10.2514/6.1994-666
42. Gross, N. Blaisdell, G.A., Lyrintzis, A.S., "Evaluation of turbulence model corrections for supersonic jets using the OVERFLOW code," AIAA–2010–4604, June, 2010. https://doi.org/10.2514/6.2010-4604
43. Feng, T. and McGuirk, J.J., "Measurements in the annular shear layer of high subsonic and under expanded round jets," *Exp. In Fluids*, Vol. 57, No. 7, 2016. https://doi.org/10.1007/s00348-015-2090-8